iScience

Article

The transcription factor IID subunit Taf13 is dispensable for TATA binding protein promoter recruitment and RNA polymerase II transcription

Graphical abstract

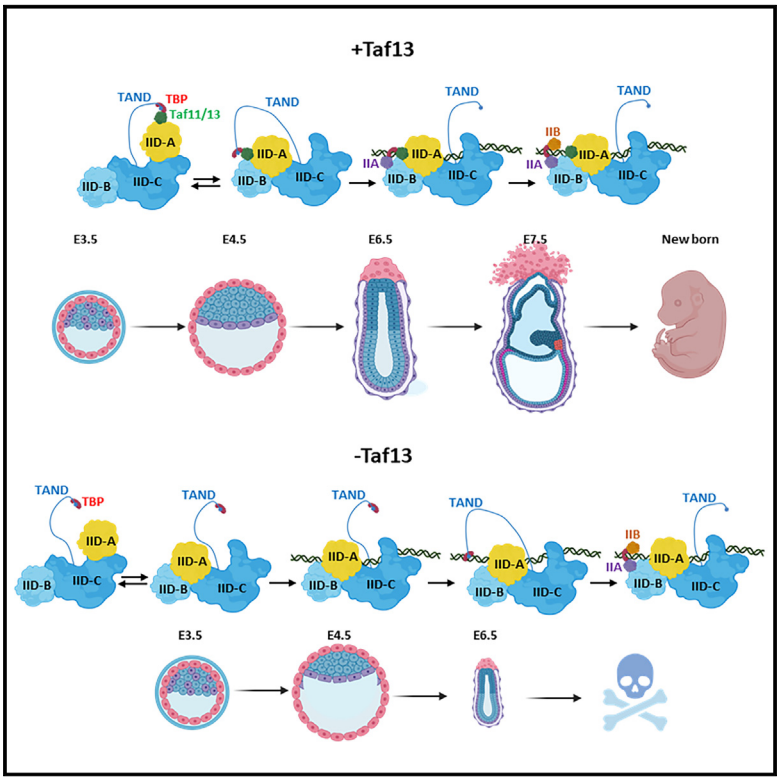

Highlights

- Taf13-null embryos fail to undergo gastrulation, leading to embryonic lethality
- Taf13-null embryonic stem cells are viable, but fail to differentiate
- TFIID integrity and TBP promoter recruitment are only mildly affected by Taf13 loss
- RNA polymerase II recruitment is globally reduced upon Taf13 loss

Authors

Igor Martianov, Stephanie Le Gras, Guillaume Davidson, Irwin Davidson

Correspondence

martiano@igbmc.fr

In brief

Biochemistry; Molecular biology; Developmental biology; Embryology

Martianov et al., 2025, iScience *28*, 112286
June 20, 2025
https://doi.org/10.1016/j.isci.2025.112286

CellPress

iScience

CellPress
OPEN ACCESS

Article

The transcription factor IID subunit Taf13 is dispensable for TATA binding protein promoter recruitment and RNA polymerase II transcription

Igor Martianov,[1,2,3,4,6,*] Stephanie Le Gras,[1,2,3,4,5] Guillaume Davidson,[1,2,3,4] and Irwin Davidson[1,2,3,4]
[1]Institut de Génétique et de Biologie Moléculaire et Cellulaire, BP 163, 67404 Illkirch, France
[2]Centre National de la Recherche Scientifique, UMR7104, 67404 Illkirch, France
[3]Institut National de la Santé et de la Recherche Médicale, U1258, 67404 Illkirch, France
[4]Université de Strasbourg, 67404 Illkirch, France
[5]GenomEast Sequencing Platform, 67404 Illkirch, France
[6]Lead contact
*Correspondence: martiano@igbmc.fr
https://doi.org/10.1016/j.isci.2025.112286

SUMMARY

The multiprotein complex TFIID, comprising the TATA binding protein (TBP) and 13 TBP-associated factors (TAFs), is an essential component of the RNA polymerase II (Pol II) preinitiation complex (PIC). Cryo-electron microscopy studies suggested a critical role of the TAF11-TAF13 heterodimer in TBP promoter deposition upstream of the transcription start site. To investigate this hypothesis, we inactivated the gene encoding Taf13 in mice and embryonic stem cells (ESCs). Taf13-null embryos implant and survive until E6.5, but fail to undergo gastrulation, while Taf13-null ESCs are viable, but fail to form embryoid bodies and differentiate. Taf13 loss had little effect on TFIID integrity and led to only a mild reduction of TBP promoter recruitment, but led to altered PIC formation and globally reduced Pol II recruitment. Thus, the Taf11-Taf13 heterodimer is not essential for TBP/TFIID recruitment, revealing plasticity in the pathways of PIC formation.

INTRODUCTION

Accurate initiation of RNA polymerase II (Pol II) transcription involves the regulated assembly of the pre-initiation complex (PIC) by the general transcription factors and Pol II on the core promoter. PIC formation is thought to be initiated by binding of the multi-subunit transcription complex TFIID comprising the TATA-box binding protein (TBP) and 13–14 TBP-associated factors (TAFs).[1–4] Electron microscopy studies showed that TFIID is organized in three lobes A-C that undergo topological reorganization during the initial steps of PIC formation.[5–11] TFIID has been proposed to adopt several conformational states as it engages the DNA and deposits TBP on both TATA-containing and TATA-less (with no consensus TATA-element) promoters.[1,12] Patel et al., proposed several TFIID conformations, canonical, extended, scanning, rearranged, and engaged during PIC formation.[13,14] A more recent study by Chen et al.,[15] defined several TFIID conformations; canonical for the unbound TFIID, the rearranged (TBP preloading), the initial TBP loading (Itl), and post-TBP loading (Ptl) forms. In each study, the conformational changes define how the structure of unbound TFIID is modified upon promoter binding, TBP deposition, and interaction with TFIIA and TFIIB. For the sake of simplicity, we will henceforth use the Chen et al. nomenclature.

A critical step in PIC assembly is the deposition and binding of TBP on the promoter DNA and its interactions with TFIIA and TFIIB, all of which are negatively regulated by the competitive binding of TAFs to TBP. The N-terminal TAND1 domain of TAF1 binds the concave DNA binding surface of TBP and blocks its DNA binding, while the TAND2 domain binds the convex surface, blocking its interaction with TFIIA.[16–18] Subsequently, it was shown that TBP interaction with the TAF11-TAF13 histone fold heterodimer also inhibits its DNA binding.[19]

The above contacts inhibit non-specific TBP-DNA interactions, finely regulating this initial step of PIC formation, but have to be relieved to allow TBP promoter binding and PIC assembly. TFIID-promoter interaction and TBP deposition involve transition from the unbound canonical to the rearranged and Itl states that repositions the TBP-containing lobe A to facilitate DNA binding, while lobe C locates further downstream with TAF1 contacting the Initiator (Inr) element spanning the transcriptional start site (TSS) and making extensive contacts with the downstream MTE and DPE elements.[15] Upon TBP promoter binding, the DNA displaces TAND1, and subsequent interaction with TFIIA displaces TAND2, reflected in the Ptl conformation, where lobe A dissociates from the promoter and reassociates with lobe C to avoid steric clash with TFIIB and Pol II. During this topological reorganization, the last contact of TBP with TFIID is via the TAF13-TAF11 heterodimer in lobe A, an interaction that finally must be released to avoid steric clash with TFIIB and is displaced by TBP-induced DNA bending.

Table 1. Genotypes of dissected E3.5- E8.5 embryos from heterozygote mating

Gestational stage	Taf13$^{+/+}$	Taf13$^{+/-}$	Taf13$^{-/-}$	Genotype
E3.5	9 (23%)	20 (50%)	11 (27%)	**#mice (%)**
E6.5	25 (20%)	70 (57%)	28 (23%)	**#mice (%)**
E7.5	10 (22%)	28 (62%)	7 (16%)	**#mice (%)**
E8.5	11 (27.5%)	26 (65%)	3 (7.5%)	**#mice (%)**

The TAF11-TAF13 heterodimer is not assembled in lobe B due to steric hindrance by switch regions in TAF6 and TAF4, while binding of the TBP-TAF11-TAF13 module is stabilized in lobe A by the presence of TAF3 that alters the placement of these switch regions.[14,15] A similar situation is seen in SAGA, where the switch domains of TAF6 and ADA1 are positioned peripherally to the core, allowing the incorporation of SPT3.[20,21] SPT3 comprises histone fold domains analogous to those of TAF11-TAF13 and is also thought to be involved in SAGA-mediated TBP loading.[22,23] Hence, lobe A organization seems designed to promote the integration of the TBP-TAF11-TAF13 module consistent with the critical role of the TAF11-TAF13 heterodimer in TBP deposition by maintaining TFIID-TBP contact after the dissociation of the TAF1-TAND1/2-TBP interactions and repositioning of lobe C in the rearranged and Itl states.

To evaluate the role of the TAF11-TAF13 heterodimer in PIC formation and transcription, we generated *Taf13*$^{-/-}$ mouse embryos and embryonic stem cells (ESCs). We found that while Taf13 was essential during embryogenesis, *Taf13*$^{-/-}$ ESCs were viable, but did not properly differentiate. Biochemical analyses showed that Taf13 loss had minimal effect on TFIID integrity at low ionic strength, but partially destabilized TFIID at higher ionic strength. Genomic profiling showed only a mild reduction of promoter recruitment of TBP and Taf4, while that of Taf1 is increased, but TFIIH recruitment was unaffected. In contrast, Pol II recruitment was globally diminished by Taf13 loss, indicating that the Taf11-Taf13 heterodimer was essential for this process.

RESULTS

Early post implantation lethality of *Taf13*$^{-/-}$ embryos

Taf13-null mice were generated by the injection of CRISPR-Cas9 RNA in fertilized oocytes with guide RNAs targeting the deletion of *Taf13* exon 3 (see STAR Methods), leading to an open reading frame with only 35 of the 124 Taf13 amino acids and completely lacking the histone fold domain. Mice carrying the *Taf13* alleles with the deletion of exon 3 were identified, and germ line transmission of the mutated allele was assessed by PCR. The resulting *Taf13* heterozygous mice were fertile and phenotypically normal. In contrast, no viable *Taf13*-null homozygous mice were born from heterozygote inter-crosses, indicating that *Taf13* inactivation is embryonic lethal. To determine at what stage *Taf13*$^{-/-}$ embryos were dying, we sacrificed mothers from heterozygous inter-crosses at different gestation stages and genotyped the dissected embryos. At embryonic stage E3.5 (early to mid-blastocyst stage), embryos were found at proper Mendelian ratios and no observable differences were found between *Taf13*$^{+/+}$ and *Taf13* $^{-/-}$ blastocysts (Table 1 and data not shown). At embryonic stage E6.5, embryos were found at expected Mendelian ratio (Table 1), but *Taf13*$^{-/-}$ embryos were characterized by their smaller size. Indeed, the mean egg cylinder length (H) of wild type embryos was 334 μM and varied from 200 to 540 μM. In contrast, for *Taf13*$^{-/-}$ mean egg cylinder length was 195 and varied from 150 to 250 (Figure 1A). At E7.5, the percentage of null embryos was reduced, and by E8.5, the majority of null embryos were no longer viable (Table 1).

To better characterize the phenotype, we performed histological sections of decidua extracted from the uterus of gestating mothers at E6.5. Embryos could be classified according to their size as normal (presumptive WT/heterozygotes, egg cylinder length above 200 μM) or small (presumptive Taf13$^{-/-}$, egg cylinder length below 200 μM). Although the embryos used for histology could not be genotyped, all analogous dissected E6.5 embryos under 200 μM length were genotyped as *Taf13*$^{-/-}$, suggesting that the small embryos seen on histological sections were also mutants. The most striking feature of small embryos was the size of epiblast (h) (Figures 1A and 1B) that varied from 50 to 100 μM with a mean value of 67 μM compared to a mean value of 204 μM of wild type littermates varying from 110 to 270 μM, with no sign of gastrulation. In contrast, the presumptive mutant embryos did not display visible histological defects of the visceral and parietal endoderm as well as extraembryonic ectoderm (Figure 1B). Histological analysis of E7.5 embryos revealed almost no progression in the development of *Taf13*$^{-/-}$ embryos compared to E6.5, with a lack of most embryonic tissue and presence of only extraembryonic tissues (Figure 1B, lower panels).

To strengthen these observations, we performed staining with markers of different cell types of early post implantation embryos. First, we stained sections with anti-Dab2 antibodies as a marker of visceral endoderm and anti-Cdx2 as a marker of extra embryonic ectoderm. Staining with these antibodies revealed the comparable presence of both these layers in the presumptive WT or *Taf13*-null embryos (Figure 1C). In contrast, staining for Oct4 as a marker of pluripotent epiblast cells showed a potent decrease of this population. This was confirmed by whole mount *in situ* hybridization of dissected and genotyped E6.5 embryos, where Oct4 signal was detected in *Taf13*$^{-/-}$ embryos, but the stained epiblast was much smaller than in wild type and heterozygous littermates (Figures 1A and 1D). Bmp4, another marker of extraembryonic ectoderm, is first expressed throughout the non-cavitated distal extraembryonic ectoderm in E5.5 embryos, and its expression persists in the extraembryonic ectoderm in a ring that abuts the epiblast in E6.5 embryos.[24] We detected Bmp4 RNA expression in 3 out of 4 null embryos, showing a heterogeneous phenotype (Figure S1A). Despite the detection of Cdx2 in all presumptive Taf13$^{-/-}$ embryos, the absence of Bmp4 in some null embryos indicated that their extraembryonic ectoderm was also defective and hence unable to assure signaling for proper embryo development.

Histological analysis did not reveal signs of gastrulation in mutant embryos. This observation was confirmed by whole mount Brachyury staining. Out of 9 null embryos, 6 did not show any Brachyury staining (Figure S1B). In 3 of the null

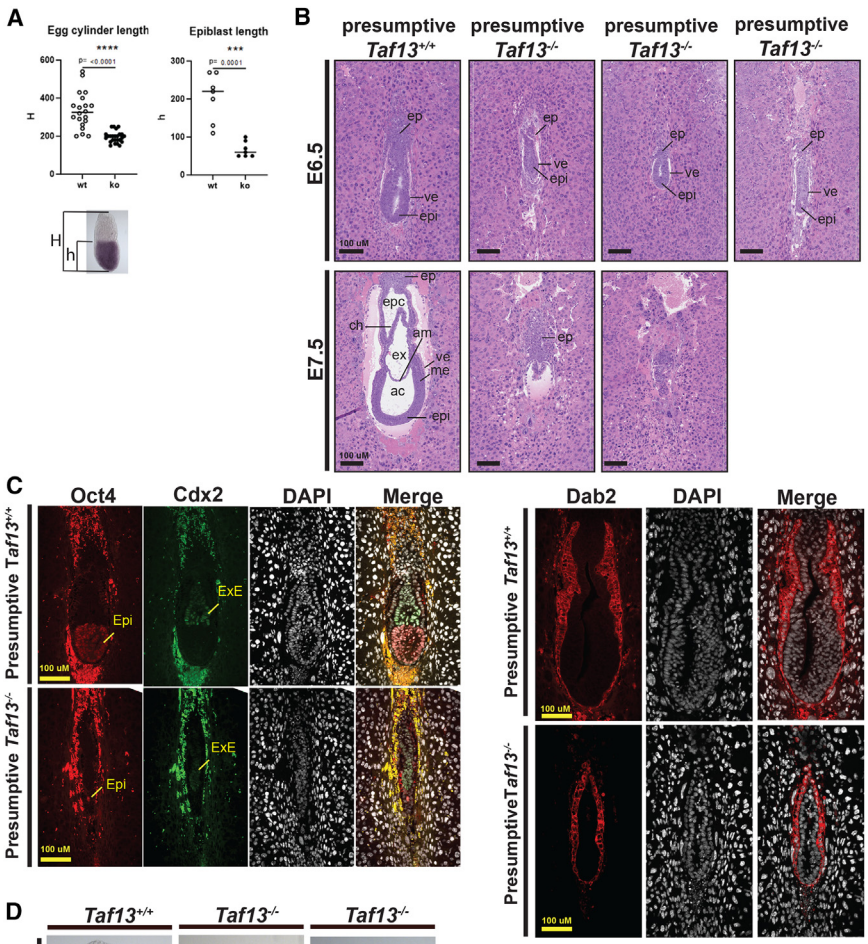

Figure 1. Early post implantation lethality of *Taf13*$^{-/-}$ embryos

(A) Egg cylinder length (H) and epiblast length (h) comparison between WT and KO E6.5 embryos. Each point represents an egg cylinder length or an epiblast length of individual embryos measured as shown in the example embryo picture. Egg cylinder length (H), WT: $n = 20$, KO: $n = 25$; epiblast length (h), WT: $n = 7$, KO: $n = 7$. Unpaired t-test equal variance. *** p-value = [0.0001, 0.001], **** p-value <0.0001. Sex of the embryos was not determined.

(B) Hematoxylin and eosin-stained sections through WT or mutant embryos at the indicated stages. ep, ectoplacental cone; ve, visceral endoderm; epi, epiblast; me, mesoderm; epc, ectoplacental cavity; ch, chorion; ex, exocoelomic cavity; am, amnion; ac, amniotic cavity.

(C) Labeling of E6.5 embryo sections with anti-Oct4, Cdx2, and Dab2 antibodies.

(D) Whole mount *in situ* hybridization of E6.5 embryos with probe against Oct4 RNA. Scale bars, 100 μm (B, C, and D).

embryos, faint staining was observed in the extra-embryonic ectoderm region, similar to E5.5 WT embryos as described.[25]

We also performed staining to detect Cer1 RNA as a marker of anterior visceral endoderm (AVE). Cer1 expression is initiated in primitive endoderm (PrE) cells in the pre-implantation blastocysts at E4.25.[26] Later during development, it is expressed in cells of distal visceral endoderm (DVE) in E5.5 embryos. These cells then migrate to the proximal anterior part of the embryo to form AVE at the E6.5 stage and continue to express Cer1.[27] Three of 7 null embryos did not express Cer1, and in 2 of 4 Cer1 expressing embryos, Cer1 was detected in the distal region, similar to E5.5 embryos. In the remaining 2 embryos, Cer1 was expressed in the anterior region, showing that cells of DVE had migrated similar to E6.5 embryos to establish the anterior-posterior axis (Figure S1C).

We further studied embryos at E4.5 when blastocysts start implantation and the inner cell mass is reorganized to form pluripotent epiblast and PrE with the epiblast encapsulated between the PE and trophectoderm. We checked if there was already any difference between *Taf13*$^{-/-}$ and *Taf13*$^{+/+}$ blastocysts at this stage by collecting blastocysts at E3.5 and culturing them for 24 h in embryonic medium. Blastocysts were fixed and stained with anti-Nanog (epiblast marker), anti-Cdx2 (trophectoderm marker), and anti-Sox17 (PrE marker) antibodies along with DAPI nuclear staining (Figures 2A and 2B). Counting the number of cells in each layer showed that epiblast and PrE were mildly but significantly reduced in *Taf13*$^{-/-}$ embryos, whereas trophectoderm cells were increased (Figure 2C).

Together, these observations showed that Taf13 was partially dispensable for the development of extra-embryonic tissue, but essential for the development of the epiblast, with mild defects seen already at E4.5, an arrest of development at E6.5, an absence of gastrulation and resorption between E7.5 and E8.5.

Taf13$^{-/-}$ embryonic stem cells are viable

The early embryonic lethality of *Taf13*$^{-/-}$ embryos precludes biochemical and functional analysis of Taf13 in developing embryos. To overcome this, we created a *Taf13*$^{-/-}$ ESC line using CRISPR-Cas9 with guide RNAs to delete exon 3, analogous to the null mice. The CRISPR-Cas9 knockout was performed concomitantly with the transfection of a vector expressing 3XHA-tagged Taf13 (3XHA-Taf13) in a doxycycline (Dox) dependent manner. Cell clones with homozygous exon 3 deletion, but expressing 3XHA-Taf13, were isolated. In these cells, the expression of the endogenous Taf13 was lost, but the expression level of exogenous 3XHA-Taf13 in *Taf13*$^{-/-}$ cells

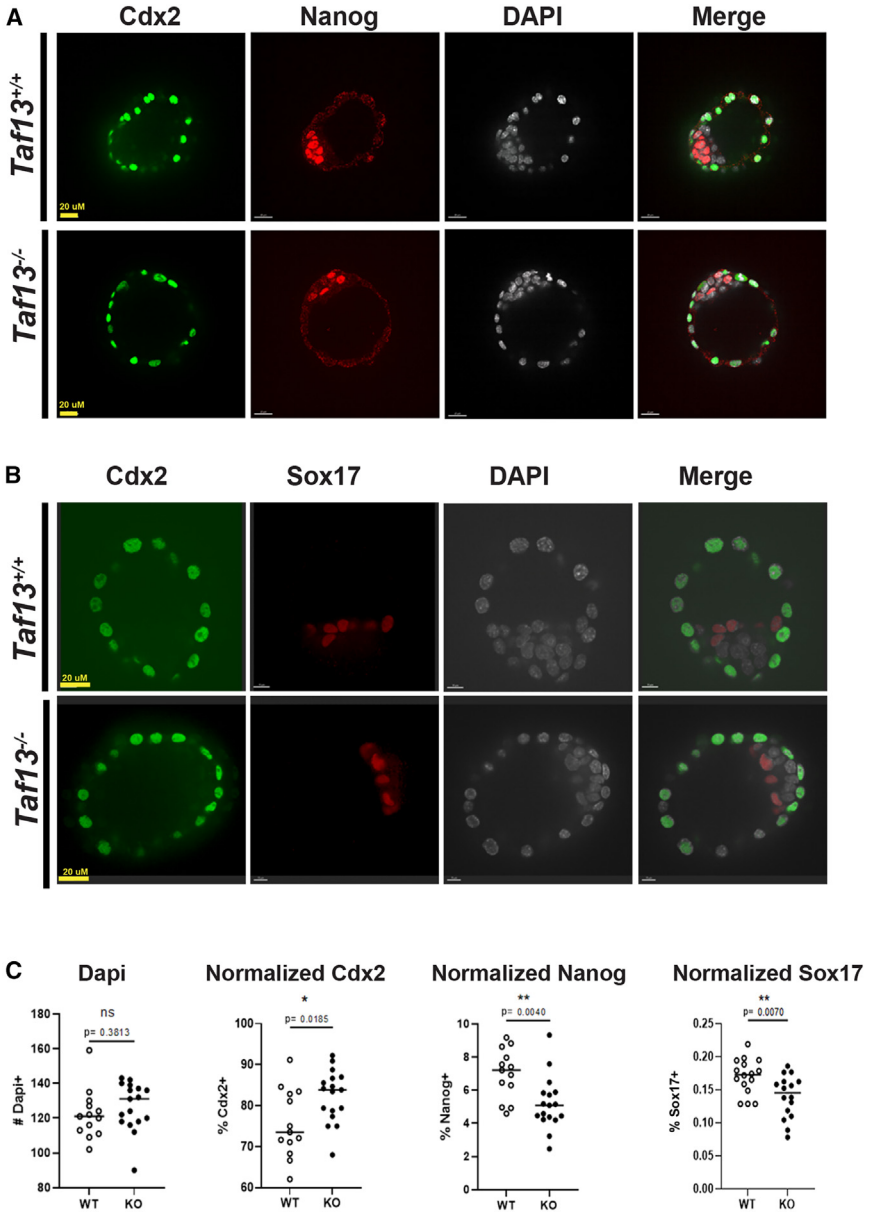

Figure 2. Reduced epiblast cell numbers in *Taf13*$^{-/-}$ E4.5 blastocysts

(A) Labeling of blastocysts with anti-Cdx2 and Nanog antibodies.

(B) Labeling of blastocysts with anti-Cdx2 and Sox17 antibodies.

(C) Comparison of cell number composing each layer in WT and *Taf13*$^{-/-}$ E4.5 blastocysts. Dapi labels all nuclei in blastocyst. Total number of cells of each blastocyst is represented by an individual point. Cdx2, Nanog, and Sox17 label trophectoderm, epiblast, and primitive endoderm, respectively. Percentage of positively labeled cells from the total cell number was calculated for each blastocyst and plotted. DAPI, Cdx2 and Nanog, WT: $n = 13$, KO: $n = 17$. Sox17, WT: $n = 16$, KO: $n = 16$. Unpaired t-test equal variance. * p-value = [0.01, 0.05], ** p-value = [0.001, 0.01], ns p-value> 0.05. Sex of the embryos was not determined. Scale bars, 20 μm (A and B).

was similar to endogenous Taf13 expression in the initial WT ESC line (Figure 3A), and the morphology of cells was unchanged (data not shown). Dox was then removed from the culture medium, leading to the extinction of 3XHA-Taf13 expression after one week.

The *Taf13*-null cells continued to proliferate in the absence of Dox for at least two weeks and did not show any change in morphology (Figure 3B), but grew more slowly than the 3XHA-Taf13 expressing cells, requiring less frequent passage and less dilution upon passage (data not shown). To quantify proliferation, we performed EdU incorporation by labeling cells for 2h before flow cytometry analyses. Compared to Taf13-expressing cells with 75,8% Alexa 488 positive cells, 64,6% Alexa 488 positive cells were detected with *Taf13*$^{-/-}$ ESCs (Figure 3C). Thus, TAF13-null ESCs were viable, but showed lower proliferation than Taf13 expressing ESCs.

To better characterize these cells, we performed bulk mRNA-seq comparing the Taf13 expressing and null lines. This analysis showed that loss of TAF13 resulted in a greater than the 2-fold upregulation of 562 genes, with only 41 up-regulated more than 4-fold. On the other hand, 382 genes were down-regulated, 34 of which showed more than a 4-fold repression (Figure 3D; Tables S1 and S2). Ontology analyses showed that the affected genes did not belong to any specific pathway (data not shown), but we noticed that many PrE markers were up-regulated by TAF13 deficiency (*Sox7*, *Sox17*, *Gata4*, *Gata6*) while several ESC markers (*Nanog*, *Klf4*, *Zfp42*) were down-regulated, but the pluripotency markers *Sox2* and *Oct3/4* were unchanged. It is important to notice that a few genes were completely repressed or *de novo* activated in the presence or absence of Taf13. Hence, Taf13 loss seemed to modulate transcription levels rather than activate or repress subsets of genes at least under these conditions.

Taf13$^{-/-}$ embryonic stem cells do not form embryoid bodies, but differentiate into epiblast-like cells

We investigated the capacity of the Taf13-null ESCs to spontaneously differentiate. *Taf13*$^{-/-}$ cells expressing or not exogenous tagged Taf13 were plated in non-adherent Petri dishes to grow as embryoid bodies (EB) over 10 days. Taf13-expressing cells readily formed EBs at day 2 and continued to grow and differentiate (Figure 4A). In contrast, Taf13-null cells failed to form EBs, and the majority of cells rapidly died. The rare cell

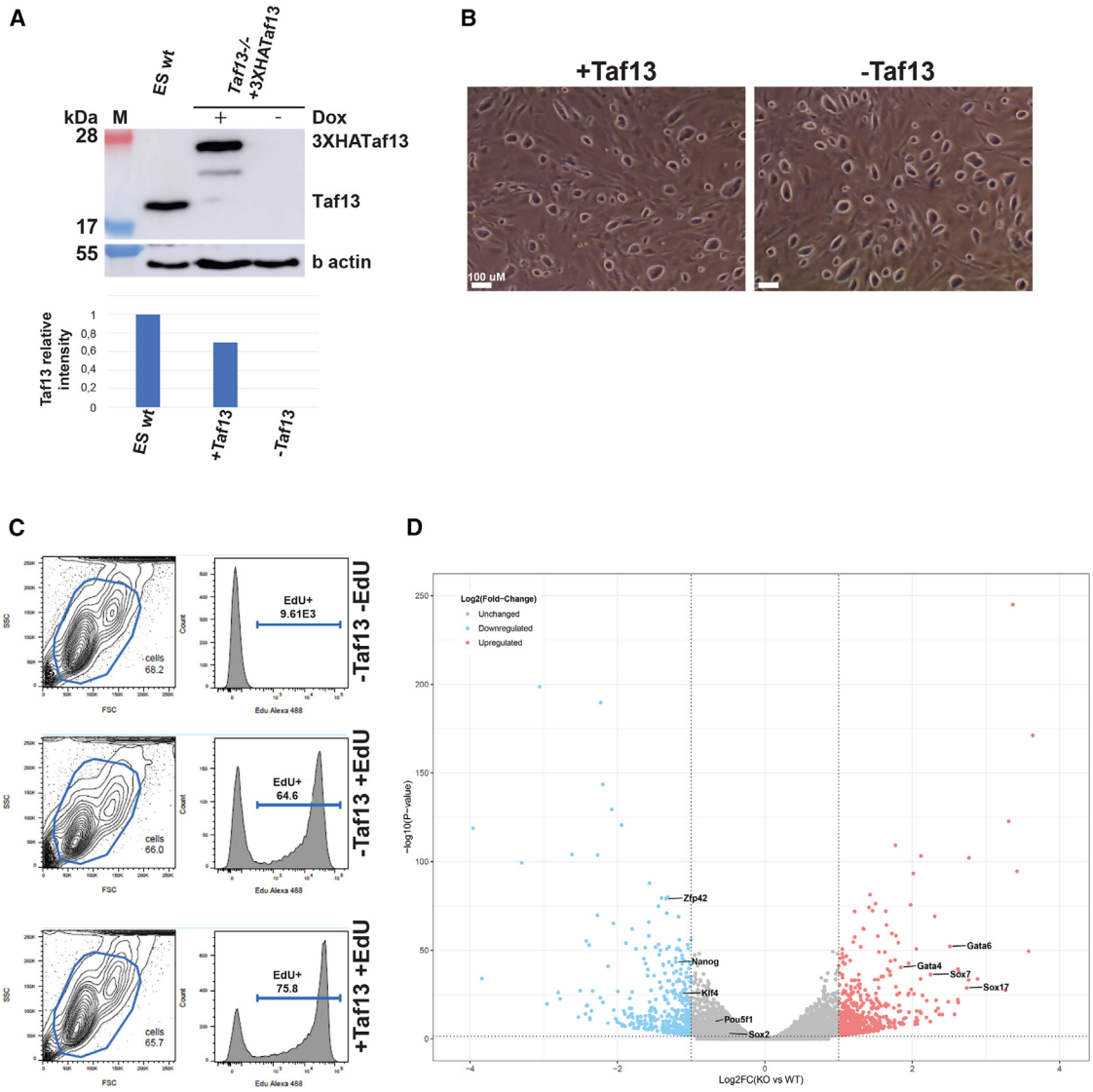

Figure 3. *Taf13*$^{-/-}$ ESC are viable

(A) Immunoblots show the absence of endogenous Taf13 in Taf13-null ESCs and expression of exogenous HA tagged Taf13 in doxycycline treated cells. Lower panel shows densitometric quantification normalized to that of b-actin. M, molecular mass marker.

(B) Phase contrast images (×5 magnification) of ESC colonies growing in the absence or presence of the doxycycline for 14 days.

(C) Cells were analyzed by FACS, and the percentage of EdU incorporation was calculated. The upper panel shows cells grown without EdU and doxycycline as a control for auto-fluorescence level.

(D) Global comparison of mRNA-seq data in Taf13 expressing and null cells. Volcano plot is shown with key PrE and pluripotency markers highlighted. Scale bars, 100 μm (B).

aggregates present at day 2 did not proliferate and were completely absent at day 8 (Figure 4A). ESCs lacking Taf13 were therefore unable to form EBs and undergo subsequent spontaneous differentiation into multiple lineages. This result also recapitulated to some extent the phenotype of the *Taf13*$^{-/-}$ embryos, where pluripotent epiblast cells did not give rise to the three primary germ layers.

In the embryo, the epiblast itself results from the differentiation of the ICM. Epiblast cells of E6.5 embryos are pluripotent, but they differ from ICM cells of blastocysts in their gene expression and their incapacity to give rise to the extraembryonic, primitive endodermal, and trophectodermal lineages.[28] This state is commonly called restricted or primed pluripotency, in contrast to the naive state of ICM cells. The differentiation of ICM into epiblast can be reconstituted *in vitro* by exposing ESCs in the naive state to Fgf2 and Activin A, differentiating them into epiblast like cells (EpiLCs).[29,30]

To differentiate *Taf13*$^{-/-}$ null ESCs into EpiLCs, we first created a population of ESC in naive state by culturing in 2i serum-free medium. We amplified ESCs expressing or not

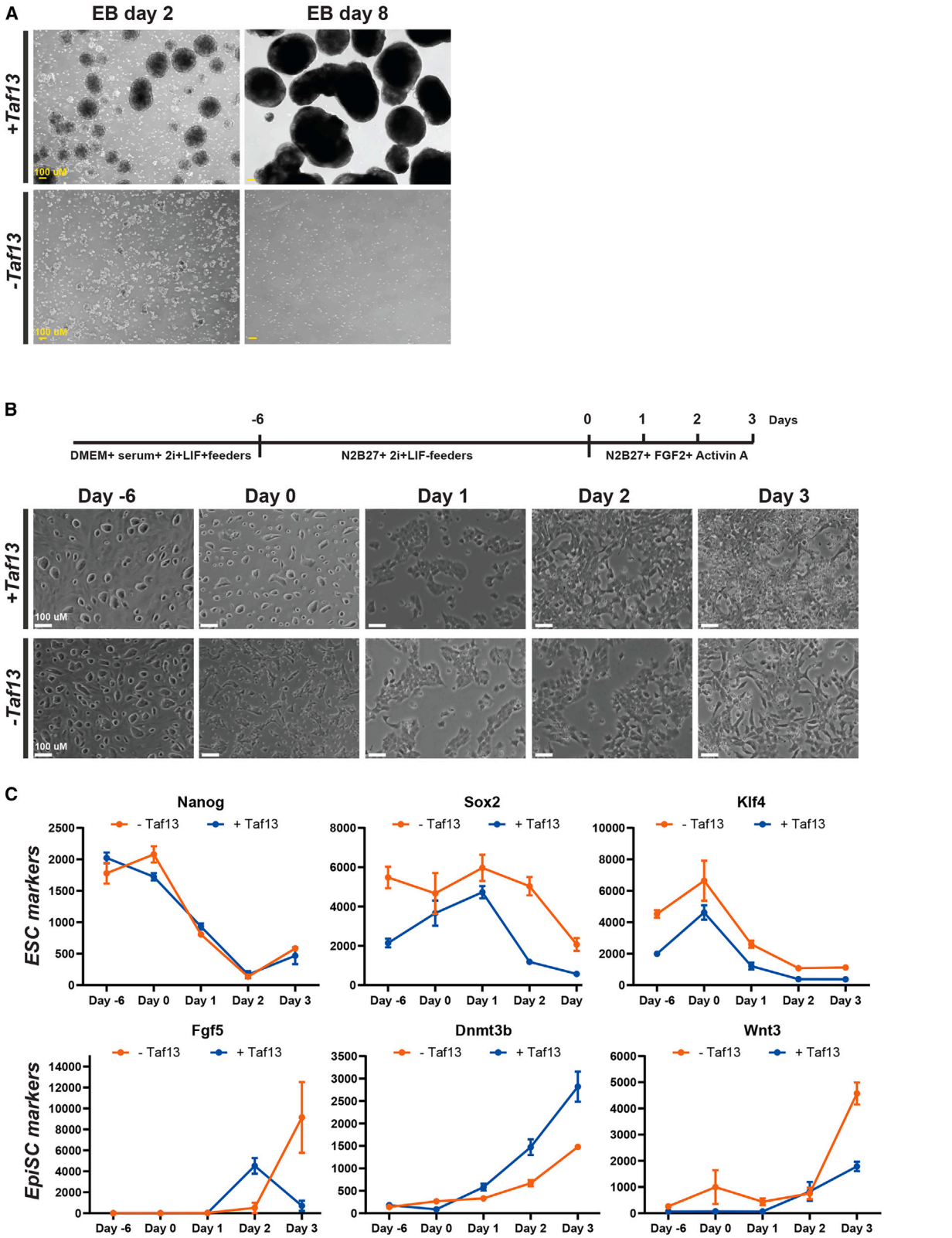

(legend on next page)

Taf13 in classic ES medium supplemented with 2i on a feeder layer and plated them in 2i medium without feeders. After 6 days in 2i medium, Taf13-expressing cells formed rounded colonies with morphology corresponding to naive ESC (Figure 4B). In contrast, ESCs lacking Taf13 formed flattened, more spread, and irregular colonies. Cells were then exposed to Fgf2 and Activin A, with both lines changing their morphology to adopt that of EpiLCs with no visible differences between the Taf13-expressing and lacking lines (Figure 4B). Cells were kept in culture for a further 3 days, but Taf13-expressing cells proliferated faster than the Taf13-null line and became quickly confluent with extensive cell death. Differentiation into EpiLCs was assessed by the expression of key marker genes. ESC markers *Nanog*, *Sox2,* and *Klf4* were down-regulated in a comparable manner in both lines, while Epiblast Stem Cells markers *Fgf5*, *Dnmt3b,* and *Wnt3* were upregulated, although the profile for Fgf5 was different between the two lines. Altogether, our results showed that Taf13 was dispensable for ESC cell viability and differentiation into EpiLCs, but was required for EB formation.

We noted that during the differentiation of ESC into EpiLCs, *Fgf5* and *Wnt3*, barely expressed in ESCs, were activated and expressed in the EpiLCs, indicating that Taf13 was not essential for *de novo* transcription activation. To investigate this, we assessed the *de novo* activation of genes in response to retinoic acid (RA) that activates the expression of a group of genes via the RA receptors (RARs) in ESCs. We cultured ESCs expressing or not Taf13 in medium containing RA for 2 days and used RT-qPCR to profile the expression of genes previously reported to be upregulated by RARs. The *Rarb*, *Lefty1*, and *Cdx1* genes were upregulated by RA in Taf13-expressing and -lacking lines (Figure S2). *Rarb* and *Lefty1* were activated *de novo* as no expression was detected in the absence of RA, whereas *Cdx1* was expressed at very low levels in the absence of RA, but strongly upregulated in its presence. The expression of these genes reached comparable levels in the absence of Taf13, but with differing kinetics, with notably a more rapid activation of *Lefty1* and *Cdx1* in the absence of Taf13. These data show that Taf13 was dispensable for *de novo* gene activation.

Taf13 inactivation destabilizes transcription factor IID, facilitating the dissociation of the TATA binding protein/Taf1/Taf7 module

As Taf13 null ESCs were viable, they offered an opportunity to investigate the biochemical consequences of loss of the Taf13-Taf11 heterodimer on TFIID integrity. As mentioned in the introduction, the Taf11-Taf13 heterodimer is present in lobe A and bridges TBP with the rest of TFIID in the rearranged and Itl states. To investigate the effects of heterodimer loss, we performed anti-TBP immunoprecipitation (IP) from extracts prepared from ESCs with or without Taf13. IPs were washed at 0.15 M KCl or 0.5 M KCl buffer. At low ionic strength, comparable to physiological conditions, lower amounts of Taf4, Taf10, and Taf12 were coprecipitated with TBP from Taf13-lacking cell extracts, whereas levels of Taf1 and Taf7 were less affected (Figure 5A). At higher ionic strength, levels of coprecipitated Taf4, Taf10, and Taf12 were more strongly reduced, but not completely absent in the absence of Taf13, while those of Taf1 and Taf7 were also reduced, but to a lesser extent (Figure 5B).

To strengthen our findings, we performed size exclusion chromatography of nuclear extracts from Taf13-expressing and Taf13-lacking ESCs in high ionic strength. The large Holo-TFIID from the Taf13-expressing cells was eluted in the first three fractions, with all tested TAFs co-eluting together (Figure 5C). Complexes of lower molecular mass were seen in particular for TAF7, as previously observed,[31] and for TBP present in multiple complexes, including those involved in Pol I and Pol III transcription. In the absence of Taf13, TAFs and TBP were depleted in the Holo-TFIID fractions 1–3 and new peaks of elution at lower molecular mass were observed (Figure 5C). TAF1 and TAF7 were depleted in fractions 1–3 and eluted as a peak in fractions 6–8. TBP was also depleted from fractions 1–3 and eluted in fractions 6–8 as well as lower molecular mass fractions. TAF4 was depleted from fractions 1–3 and eluted as a new peak in fractions 5–7 along with a part of the TAF10 and TAF12 populations. These latter TAFs are shared with SAGA-family complexes, and therefore, a sub-population remains present in the highest molecular mass fractions.

All together these experiments showed that Taf13 loss had a mild destabilizing effect on TFIID at physiological ionic strength, which was exacerbated at higher ionic strength with the partial dissociation of a TBP-Taf1-Taf7 subcomplex in lobe C from the TAF10, 4, and 12 present in lobes A and B.

Taf13 inactivation does not impair TATA binding protein/transcription factor IID promoter recruitment and polymerase II preinitiation complex formation, but reduces polymerase II recruitment

We next used ChIP-seq to analyze how loss of the Taf11-Taf13 heterodimer impacted TBP, Taf1, and Pol II recruitment. Of the 16316 promoters positive for H3K4me3, a mark of active and/or poised promoters (Figure S3A), 9554 displayed strong TBP occupancy, with the remainder showing only weak occupancy (Figure 6A). In Taf13 ESCs expressing ectopic 3HA-tagged Taf13, HA-ChIP showed that all promoters bound by TBP were also bound by Taf13 (Figure 6A). Global comparison of TBP ChIP-seq in Taf13-expressing or null ESCs showed only mild effects, with a 24% reduction seen in cluster 1 that represented the strongest bound sites (Figures 6A and 6B). In contrast, Taf1

Figure 4. *Taf13*$^{-/-}$ ESCs do not form embryoid bodies, but differentiate into epiblast-like cells

(A) Phase-contrast microscopy (5X magnification) of EBs at days 2 and 8 from 3XHA-Taf13 cells grown in the presence or absence of Dox and thus expressing or not Taf13.

(B) Morphology of differentiating indicated differentiating cells. Differentiation protocol is schematically shown on upper panel and phase-contrast images of cells was taken at indicated stages.

(C) Expression of the indicated marker genes during differentiation into EpiLC in 3XHATaf13 expressing and not expressing cells as measured by qPCR and normalized to the Oct4 transcript expressed as arbitrary units. Data are presented as mean +/− standard deviation (SD). $n = 3$ (3 technical replicates). Scale bars, 100 μm (A and B).

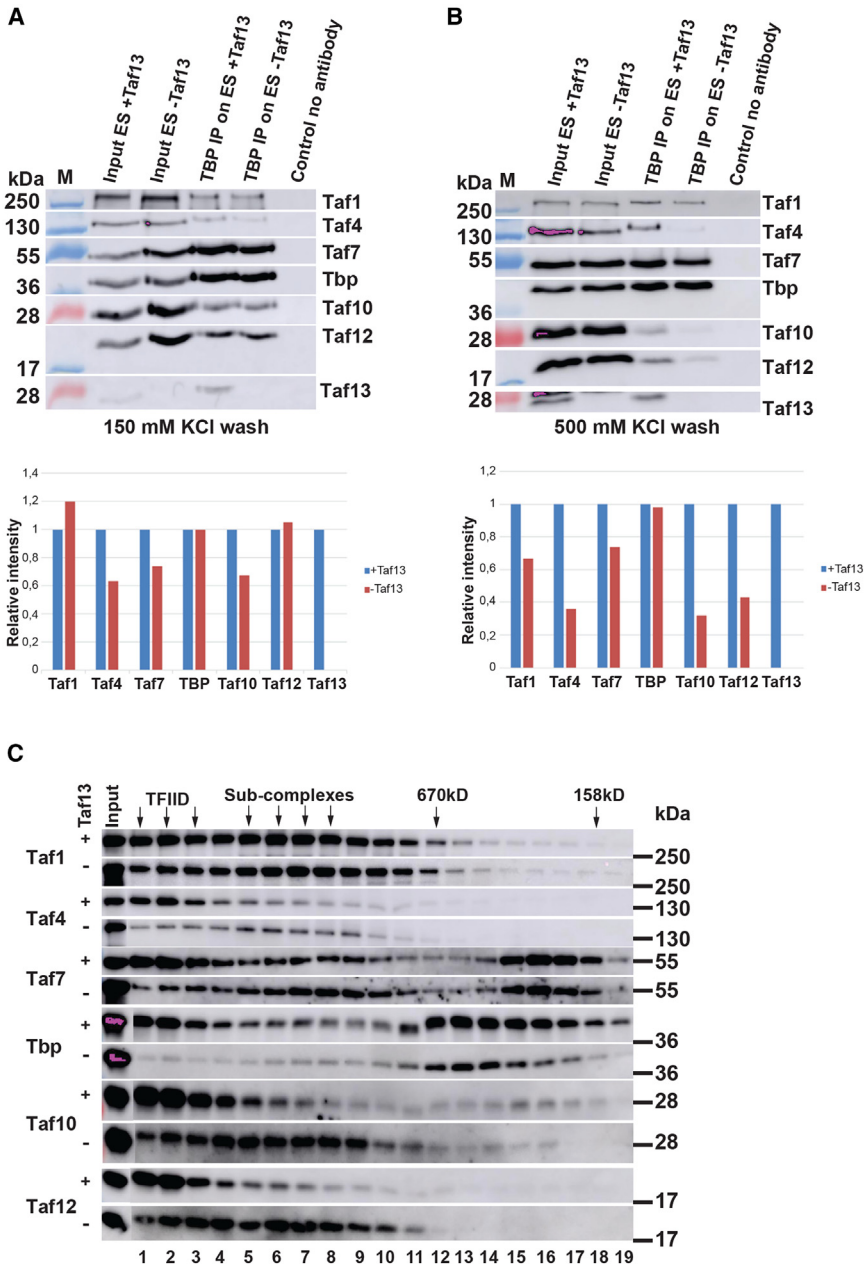

Figure 5. Taf13 inactivation destabilizes TFIID integrity, facilitating the dissociation of the TBP/Taf1/Taf7 module

(A and B) Immunoblot analyses of Tafs co-precipitated with TBP in low 150 mM KCl (A) or high 500 mM KCl (B) wash conditions (upper panel). Lower panel shows densitometric quantification. M, molecular mass marker.

(C) Immunoblots on size exclusion chromatography fractions of nuclear extracts from the indicated ESCs.

We investigated whether TBP recruitment in the presence or absence of Taf13 was impacted by the presence of a consensus TATA-element. We performed peak calling for TBP ChIP-seq in the Taf13 expressing cells, identifying 7914 peaks. A Homer search for DNA motifs at +/− 50 bp from the peak summit identified the TATA(A/T)AA sequence as the best scored motif (Figure S5A). Using this matrix, we identified 487 TATA-containing TBP peaks, of which 91 were located +/− 500 bp with respect to the annotated TSS. At these TSS, the increase in Taf1 (49%) and the decrease in Pol II (29%) were comparable to the overall values (Figures S5A and S5B). Nevertheless, for TBP, the reduction of 29% was marginally higher than overall and more comparable to that of cluster 1 (Figures 6A and 6B), corresponding to the most strongly occupied sites. 57 of the 91 TATA-containing sites were present in this cluster, the remainder being distributed amongst the other clusters (Figure 6B). The presence of the TATA element appeared to negatively impact TBP recruitment upon Taf13 loss since the value of 29% was marginally higher than the overall 24% of cluster 1 and was calculated taking into account the 34 sites in the other clusters where the overall reduction in TBP was much lower. Thus, paradoxically, TBP recruitment to the better occupied promoters and/or those enriched in TATA elements was more affected by Taf13 loss than those with no recognizable TATA elements.

levels were around 40% increased at almost all promoters. TBP and Taf1 binding was illustrated at representative promoters of clusters 1–4 (Figure 6C). These observations were confirmed by independent ChIP-qPCR experiments at the *Rplp0* and *MiR320* promoters, where TBP levels were comparable, but Taf1 levels clearly increased (Figure S4). Comparing the meta-profiles showed that in clusters 1 and 3, Taf1 peaks were observed both upstream and downstream of the TSS, but in cluster 1 strongest Taf1 peaks were seen downstream, whereas in cluster 3, they were upstream (Figure 6B). In contrast, in cluster 4, Taf1 appeared as a single peak downstream of TBP. Cluster 2 gave a more diffuse and broad profile that was less informative on the relative locations of TAF1.

To better address TFIID recruitment and PIC formation, we attempted ChIP-seq with several antibodies targeting TFIID or TFIIH subunits that failed to give robust signals in mouse (data not shown). We therefore performed Cut&tag for TBP, Taf4, and the TFIIH subunit Xpb as previously reported.[32] Strong TBP occupancy of 6777 promoters was observed, a smaller number than seen with ChIP-seq (Figure S6A). Taf4 was recruited to all these TBP occupied promoters (Figures 6A and 6B). In the absence of Taf13, a mild 11–17% reduction of TBP

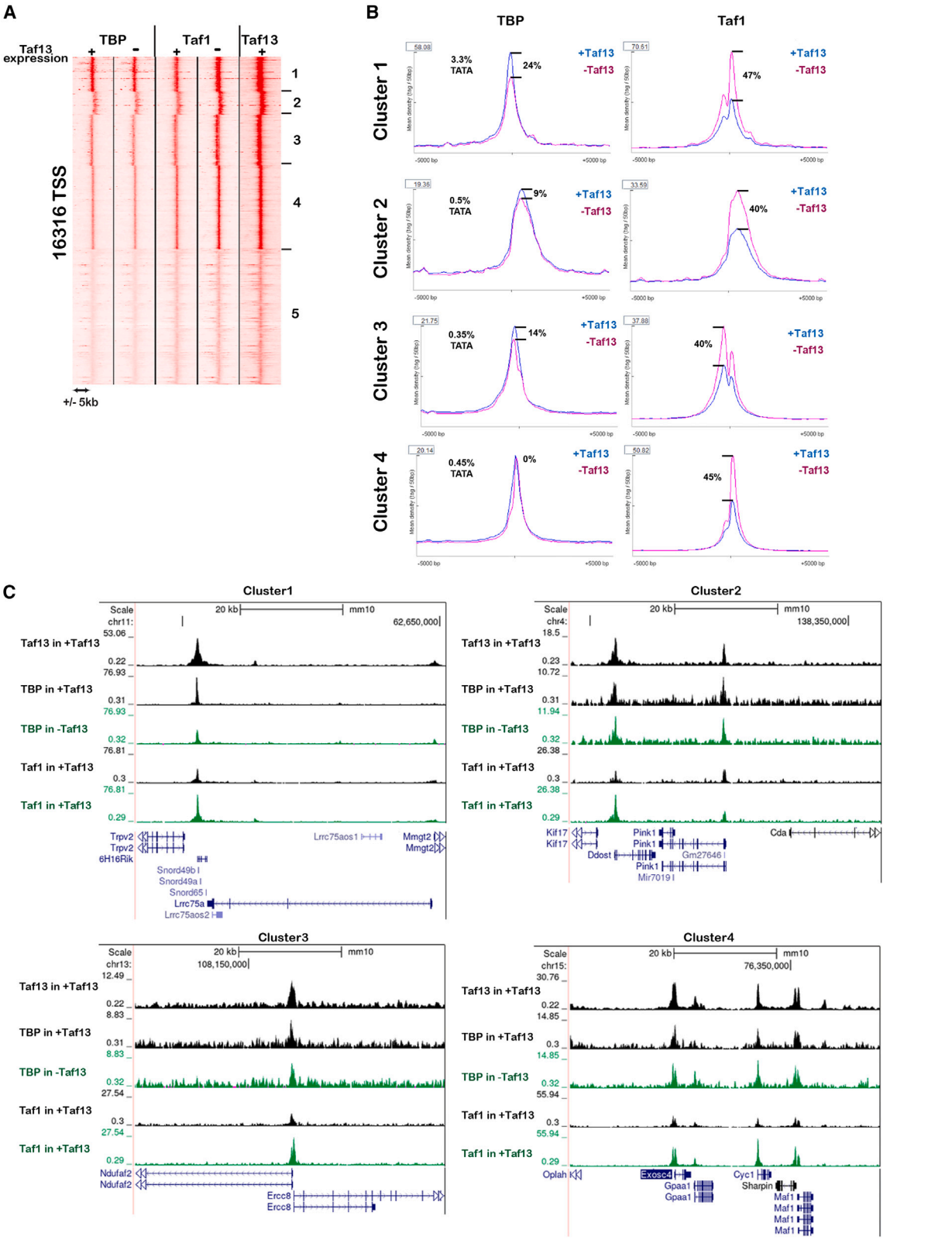

(legend on next page)

binding was observed, with a stronger 26–31% reduction of Taf4 (Figure S6C). In contrast, Xpb occupancy, also seen at all TBP-bound promoters, was not affected by Taf13 loss.

Despite the above, Pol II recruitment was notably reduced by 30–36% at almost all promoters with a high signal (Figure 7A). Clustering of the Pol II signal revealed promoters with little pausing and high levels of elongating Pol II characteristic of super-enhancer driven genes[33] (Figure 7B, Cluster 1) as well as additional clusters with differing ratios between the paused and elongating Pol II (Clusters 2–4). Meta analyses of clusters 1–4 revealed that absence of Taf13 led to a reduction in both promoter bound and elongating Pol II. ChIP-qPCR confirmed the reduction of Pol II at the *Rplp0* and *MiR320* promoters (Figure S4). No changes in the pausing indices of clusters 1 and 3 were observed, showing that both Pol II promoter recruitment and elongation were affected to comparable extents (Figure 7C). The pausing index was, however, mildly decreased in cluster 2, but could not be accurately calculated in clusters 4 and 5 due to the low Pol II signal in the gene body.

As mentioned above, Taf13 inactivation impacted gene expression with both up and down regulated genes. We performed selective analyses of TBP, Xpb, and Pol II recruitment at the promoters of the up and down-regulated genes. While TBP levels were somewhat lower at downregulated genes, Xpb showed little change (Figure S7). Nevertheless, Pol II levels in absence of Taf13 were higher at upregulated genes (i.e., less affected by Taf13 loss), with a reduction of 17% compared to more than 30% overall. In contrast, Pol II levels at downregulated genes were lower (62%) compared to overall. Hence in the absence of Taf13, upregulated genes showed increased Pol II and downregulated genes lower levels, correlating with the increased or decreased gene expression. The changes in Pol II levels at these 2 classes of promoters showed little correlation with those of TBP and Xpb. Similarly, at the TATA-containing promoters, clusters 1 and 2 showed similar TBP reduction, but Pol II levels were more strongly reduced in cluster 2. Moreover, while the clustering based on the TBP signal (Figure 6A) or that of Pol II (Figure 7A) defines distinct sets of promoters, there was no strong correlation between TBP levels reduced by 9–24% and Pol II levels reduced by 30–36%. Therefore, there was little correlation between changes in TBP/TFIID recruitment PIC formation, as assessed by Xpb levels, and Pol II levels.

We further investigated the effects of Taf13 loss on H3K27ac and H3K4me3 at promoters to assess whether the effects on TBP/TFIID and Pol recruitment affected their epigenetic marking. H3K4me3 levels were unchanged at the 16316 marked promoters (Figure S3A). Of these only 10656 displayed a high H3K27ac signal, whereas cluster 5 showed only a weak signal, likely corresponding to inactive but poised promoters. Nevertheless, H3K27ac levels were mildly increased in all clusters in the absence of Taf13. However, given this mild effect, no robust conclusions concerning cause and effect with respect to PIC formation or Pol II recruitment can be made at this stage.

Taken together, these data showed that loss of the Taf11-Taf13 heterodimer did not strongly impact TBP/TFIID recruitment to promoters or PIC formation, but rather led to reduced Pol II recruitment.

DISCUSSION

Here, we performed genetic knockout of *Taf13* to address its role in early development and TBP promoter recruitment. Our results indicated that while Taf13 was required during early embryogenesis, it was not required for mESC viability. Loss of Taf13 had only a mild impact on TBP/TFIID promoter TBP recruitment, whereas Pol II recruitment was reduced.

Taf13 loss led to growth defects in early embryos, with the highest impact seen in the epiblast, whose size was strongly reduced. The number of epiblast cells was reduced as early as E4.5, and the epiblast failed to develop normally, leading to the loss of viability by E7.5. In contrast, extra-embryonic tissue development was partially and heterogeneously affected with incomplete penetrance. While our article was under review, He et al.,[34] also independently reported highly comparable observations with reduced epiblast, maintained CDX2 expression and lack of Brachyury expression and gastrulation in Taf13$^{-/-}$ embryos.

The phenotype of Taf13$^{-/-}$ embryos was less severe than that observed upon loss of TFIID subunits Taf5, Taf7, Taf8, Taf10, Taf12, and TBP. TBP null embryos developed up to the early blastocyst stage and died before implantation.[34,35] Knock out of Taf5, Taf7, Taf8, Taf10, or Taf12 resulted in peri-implantation lethality where embryos were able to elicit a decidual response, but were able neither to implant nor expand.[34,36,37] In contrast, the development of Taf4 mutant embryos continued to a much later stage due to redundancy with its paralog Taf4b.[31] Rapid cell division required for the expansion of the epiblast, therefore, seems to be particularly sensitive to the loss of TFIID subunits, perhaps due to the requirement for the rapid PIC reformation and re-initiation of transcription following each mitosis that may be slowed or otherwise impacted by their inactivation.

Consistent with this idea, cultured Taf13-null ESCs were viable but displayed lower proliferation reminiscent of the reduced number of epiblast cells seen *in vivo*. Moreover, these ESCs could be differentiated into epiblast-like cells modeling *in vivo* differentiation of the inner cell mass to epiblast cells. In contrast, the mutant ESCs did not form EBs and therefore could not be differentiated into specified lineages. Defective EB formation cannot be simply explained by the inability to activate gene expression *de novo,* since *Fgf5* was activated during epiblast differentiation, and RA-responsive genes could also be induced upon RA treatment. Thus, while Taf13 was not necessary for the viability of undifferentiated ESCs, it was required for EB

Figure 6. Effects of Taf13 loss on promoter occupancy by TBP and Taf1

(A) Heatmap of ChIP seq signals of TBP, Taf1, and Taf13 in the indicated cells.

(B) Meta-profiles of promoter occupancy by TBP and Taf1 in the 4 clusters with significant TBP, Taf1, and Taf13 signals. The difference in average signals in Taf13 expressing and lacking cells is indicated.

(C) USCS browser tracks illustrating promoter occupancy of genes belonging to each of the 4 clusters.

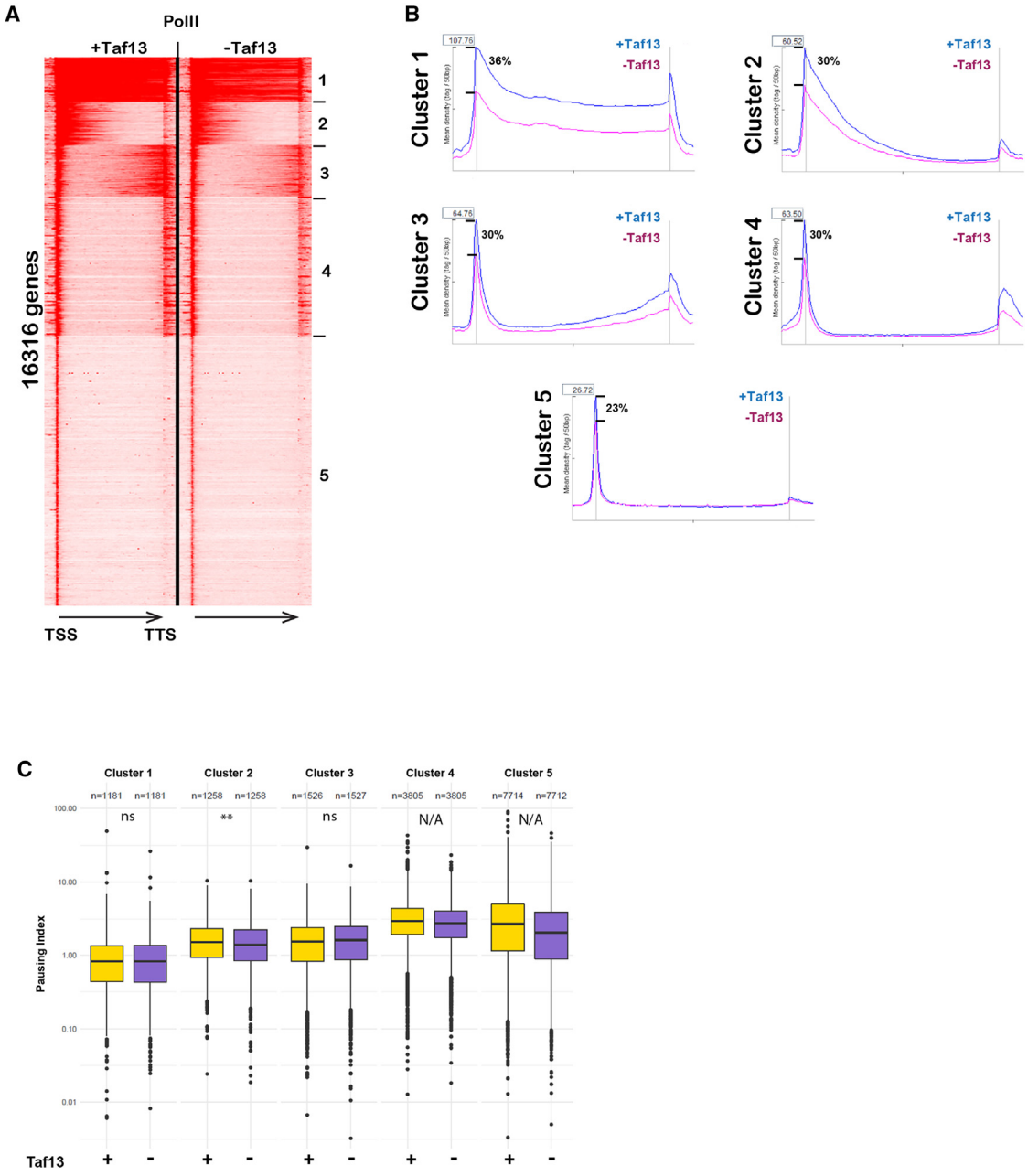

Figure 7. Decreased promoter and gene body occupancy by Pol II in the absence of Taf13

(A) Heatmap of Pol II ChIP seq signals.

(B) Meta-profiles of Pol II promoter and gene body occupancy from the transcription start site (TSS) to the transcription termination site (TTS). The difference in average signals in Taf13 expressing and lacking cells is indicated.

(C) Boxplot shows Pol II pausing index distribution in Taf13 expressing and null cells for each cluster. **p value = [0.001, 0.01], ns p value > 0.05.

formation involving major and coordinate changes in gene expression. Similarly, in humans, *TAF13* mutations that impact its ability to form heterodimers with TAF11 have specific effects on neurodevelopment, leading to microcephaly, intellectual disability, and small stature rather than lethality.[38]

Both TBP immunoprecipitation and size exclusion chromatography showed that TFIID integrity was destabilized in Taf13-null ESCs. This effect was mild at low ionic strength, but was exacerbated at higher ionic strength, where the Taf4, Taf12, and Taf10 components of the TFIID A and B lobes were less stably associated with the Taf1-Taf7-TBP module, leading to reduced levels of holo-TFIID. TFIID is thought to assemble in a hierarchical and sequential manner from co-translational steps.[6] Core TFIID comprises TAF5 and the TAF6-TAF9 and TAF4-TAF12

histone fold pairs that form the basis of the A and B lobes. Subsequent association of TAF2, TAF8-TAF10 completes B-lobe formation, and this complex can then be assembled with the nascent TAF1 peptide.

According to the known cryo-EM structures of TFIID, it is not clear why TAF11-TAF13 loss from lobe A would destabilize interactions between TAF1-TAF7 in lobe C and lobe A, although crosslinking experiments revealed that TAF1 interacts with TAF11-TAF13 via motif centered on K249 of TAF1.[6] Loss of the TAF1-TAF13-TAF11 interaction upon Taf13 inactivation may destabilize the lobe C-lobe A interactions with TBP no longer having contacts with lobe A, but being tethered to TFIID mainly through the TAF1 TAND domain. Hence, under high ionic strength, lobe A may be partially dissociated from lobe C, but lobe B-C interactions persist, explaining the residual Taf4, Taf10, and Taf12 seen in the TBP IP.

The presence of Taf4, albeit at reduced levels, at TBP-occupied promoters indicated that TBP was mainly recruited in a holo-TFIID complex or, as discussed above, at least a lobe B-Lobe C subcomplex, rather than a Taf1-Taf7-TBP complex. As described in the introduction, comprehensive analyses of stepwise PIC formation by cryo-EM proposed a mechanism for the topological reorganization of TFIID during the initial steps of PIC formation involving TBP promoter deposition. In this model, lobe A dissociates from lobe C and re-localizes to position TAF13-TAF11-TBP for promoter deposition. The TAF13-TAF11 heterodimer is hence the last component of TFIID to make direct contact with TBP. The limited impact on promoter TBP levels in cells lacking the TAF11-TAF13 heterodimer showed that, despite the above models, this heterodimer was in fact largely dispensable for TBP recruitment.

Our data suggest an alternative pathway for TBP deposition in the absence of Taf13 in which TBP is recruited to promoters via interaction with the TAND domain of Taf1. As this interaction is weaker and/or the TAND domain is potentially more flexible, the accurate deposition of TBP may be slowed and/or involve local scanning of the DNA before being properly positioned by the TAF4-TFIIA-TBP interaction. Indeed, the TAF4-TAF12 heterodimer in lobe B contacts the TFIIA-TBP complex via binding of the C-terminal TAF4 ''ABM'' region to the TFIIA helix bundle.[15] Thus, once the TAF1-TAND interaction with TBP is lost due to DNA contacts, TBP may be stabilized and positioned at the promoter indirectly by TAF4-TFIIA-TBP interaction. Moreover, TBP recruitment seemed more affected at TATA-containing promoters that rely more on TBP-TATA interactions and less on Taf1 interaction with MTE/DPE downstream elements.

This model may also explain the increased Taf1 ChIP-seq signal in the absence of Taf13. In normal PIC formation, TAF1 maintains downstream promoter binding during the initial stages of PIC assembly, but is displaced upon TFIIH binding and upon transcription initiation.[15] If PIC formation is slowed by use of an alternative, less efficient pathway for TBP deposition, Taf1 will have a longer residence time before TFIIH is recruited and Pol II initiates transcription, accounting for the higher Chip-signal. Further ChIP experiments with additional subunits of TFIID and the PIC will be required to clarify the mechanism involved.

Limitations of the study

Here, we showed that the Taf13-Taf11 heterodimer was not required for TBP promoter recruitment and transcription in mouse ESCs. Previously, it has been shown that even TBP is not required in ESCs.[32] Moreover, TBP or TAF1 depletion in human HAP1 cells also had only limited effects on Pol II transcription.[39] However, it is not clear to what extent TBP and TAF-requirements, in particular of Taf13, may differ in different cell contexts depending on their differentiation or proliferation status. As mentioned above, *TAF13* mutations in humans affect neurodevelopmental processes,[38] suggesting it is required at either a specific developmental stage or for the expression of a specific gene expression program(s). Why TAF13 or, more generally, TBP and TAFs may be required at some promoters or developmental stages, but not others, remains to be determined.

Similarly, although we showed that Taf13 was not necessary for TBP recruitment and PIC formation, from our current studies, we could not readily decipher the organization of the residual TFIID, nor the alternative pathways mediating TBP recruitment, nor how overall PIC formation may be altered. Cryo-EM has provided unprecedented understanding of how the PIC assembles when all components are present in normal cells. However, from this and previous studies, it is clear that there must be considerable flexibility in how functional PICs can assemble from partial TFIID subcomplexes or indeed how they assemble in the absence of TBP and its paralogues.[32,35,39,40] Further studies involving extensive genomic profiling for additional PIC components in cells lacking TBP or TAFs may help to better understand the plasticity of PIC formation. Perhaps, the simultaneous inactivation of Taf13 together with other Tafs or TBP would help to address this issue. Similarly, ChIP-seq studies also did not address the potential impact of Taf13 loss on the kinetics of PIC formation. Additional time resolved approaches, such as live single molecule imaging, would be required to address this.

RESOURCE AVAILABILITY

Lead contact

Requests for further information, resources, and reagents should be directed to and will be fulfilled by the lead contact, Igor Martianov (martiano@igbmc.fr).

Materials availability

Recombinant mice and ES cell lines generated in this study are available upon request and completion of an MTA.

Data and code availability

The ChIP seq, RNA seq, and cut&tag data described in this study are deposited at the GEO database with accession number GSE254025.

ACKNOWLEDGMENTS

We thank M-C. Birling and the staff at the Mouse Clinical Institute and the PHENOMIN consortium for the establishment of the Taf13 mutant mouse line. Drs N. Jung and P. Rossolillo for plasmid design and production. We acknowledge the support of the IGBMC Light Microscopy Facility imaging center and, in particular, of M. Silvin, member of the national infrastructure France-BioImaging supported by the French National Research Agency (ANR-10-INBS-04). Dr O. Wendling and the MCI histopathology service for histology. Dr M. Rhinn for assistance with embryo dissection. Dr A. Izcue for fruitful discussions and statistical analysis. This work was supported by the Ligue Nationale contre le Cancer, the Investissements d'Avenir ANR-10-IDEX-0002-02 and

ANR-10-LABX-0030-INRT French state fund. The IGBMC high throughput sequencing GenomEast facility is a member of the "France Génomique" consortium funded by ANR10-INBS-09-08; ID is an "équipe labelisée" of the Ligue Nationale contre le Cancer.

AUTHOR CONTRIBUTIONS

IM performed all cell and molecular biology experiments. SLG and GD performed the bioinformatics analyses. IM and ID designed experiments, evaluated the data, and wrote the article.

DECLARATION OF INTERESTS

The authors declare no competing interests.

STAR★METHODS

Detailed methods are provided in the online version of this paper and include the following:

- KEY RESOURCES TABLE
- EXPERIMENTAL MODEL AND STUDY PARTICIPANT DETAILS
  - Generation of Taf13 knock out mice
  - Generation of mESC lines
- METHOD DETAILS
  - Cell culture, growth and differentiation
  - Blastocyst isolation and culture
  - Histology and whole mount *in situ* hybridization
  - Immunostaining
  - Genotyping of blastocysts and later stage embryos
  - Preparation of ESC nuclear extracts, immunoprecipitation, gel filtration and immunoblot
  - RNA preparation, quantitative PCR and RNA-seq
  - Chromatin preparation, chromatin immunoprecipitation, sequencing and analysis
  - Cut & Tag
  - Pausing index
- QUANTIFICATION AND STATISTICAL ANALYSIS

SUPPLEMENTAL INFORMATION

Supplemental information can be found online at https://doi.org/10.1016/j.isci.2025.112286.

Received: May 2, 2024
Revised: November 22, 2024
Accepted: March 21, 2025
Published: May 5, 2025

REFERENCES

1. Malik, S., and Roeder, R.G. (2023). Regulation of the RNA polymerase II pre-initiation complex by its associated coactivators. Nat. Rev. Genet. *24*, 767–782. https://doi.org/10.1038/s41576-023-00630-9.
2. Roeder, R.G. (2019). 50+ years of eukaryotic transcription: an expanding universe of factors and mechanisms. Nat. Struct. Mol. Biol. *26*, 783–791. https://doi.org/10.1038/s41594-019-0287-x.
3. Farnung, L., and Vos, S.M. (2022). Assembly of RNA polymerase II transcription initiation complexes. Curr. Opin. Struct. Biol. *73*, 102335. https://doi.org/10.1016/j.sbi.2022.102335.
4. Nogales, E., Louder, R.K., and He, Y. (2017). Structural Insights into the Eukaryotic Transcription Initiation Machinery. Annu. Rev. Biophys. *46*, 59–83. https://doi.org/10.1146/annurev-biophys-070816-033751.
5. Andel, F., Ladurner, A.G., Inouye, C., Tjian, R., and Nogales, E. (1999). Three-dimensional structure of the human TFIID-IIA-IIB complex. Science *286*, 2153–2156.
6. Bernardini, A., Mukherjee, P., Scheer, E., Kamenova, I., Antonova, S., Mendoza Sanchez, P.K., Yayli, G., Morlet, B., Timmers, H.T.M., and Tora, L. (2023). Hierarchical TAF1-dependent co-translational assembly of the basal transcription factor TFIID. Nat. Struct. Mol. Biol. *30*, 1141–1152. https://doi.org/10.1038/s41594-023-01026-3.
7. Bieniossek, C., Papai, G., Schaffitzel, C., Garzoni, F., Chaillet, M., Scheer, E., Papadopoulos, P., Tora, L., Schultz, P., and Berger, I. (2013). The architecture of human general transcription factor TFIID core complex. Nature *493*, 699–702. https://doi.org/10.1038/nature11791.
8. Burley, S.K., and Roeder, R.G. (1996). Biochemistry and structural biology of transcription factor IID (TFIID). Annu. Rev. Biochem. *65*, 769–799.
9. Cler, E., Papai, G., Schultz, P., and Davidson, I. (2009). Recent advances in understanding the structure and function of general transcription factor TFIID. Cell. Mol. Life Sci. *66*, 2123–2134.
10. Kolesnikova, O., Ben-Shem, A., Luo, J., Ranish, J., Schultz, P., and Papai, G. (2018). Molecular structure of promoter-bound yeast TFIID. Nat. Commun. *9*, 4666. https://doi.org/10.1038/s41467-018-07096-y.
11. Papai, G., Weil, P.A., and Schultz, P. (2011). New insights into the function of transcription factor TFIID from recent structural studies. Curr. Opin. Genet. Dev. *21*, 219–224. https://doi.org/10.1016/j.gde.2011.01.009.
12. Bernardini, A., Hollinger, C., Willgenss, D., Müller, F., Devys, D., and Tora, L. (2023). Transcription factor IID parks and drives preinitiation complexes at sharp or broad promoters. Trends Biochem. Sci. *48*, 839–848. https://doi.org/10.1016/j.tibs.2023.07.009.
13. Patel, A.B., Greber, B.J., and Nogales, E. (2020). Recent insights into the structure of TFIID, its assembly, and its binding to core promoter. Curr. Opin. Struct. Biol. *61*, 17–24. https://doi.org/10.1016/j.sbi.2019.10.001.
14. Patel, A.B., Louder, R.K., Greber, B.J., Grünberg, S., Luo, J., Fang, J., Liu, Y., Ranish, J., Hahn, S., and Nogales, E. (2018). Structure of human TFIID and mechanism of TBP loading onto promoter DNA. Science *362*, eaau8872. https://doi.org/10.1126/science.aau8872.
15. Chen, X., Qi, Y., Wu, Z., Wang, X., Li, J., Zhao, D., Hou, H., Li, Y., Yu, Z., Liu, W., et al. (2021). Structural insights into preinitiation complex assembly on core promoters. Science *372*, eaba8490. https://doi.org/10.1126/science.aba8490.
16. Kotani, T., Miyake, T., Tsukihashi, Y., Hinnebusch, A.G., Nakatani, Y., Kawaichi, M., and Kokubo, T. (1998). Identification of highly conserved amino-terminal segments of dTAFII230 and yTAFII145 that are functionally interchangeable for inhibiting TBP- DNA interactions *in vitro* and in promoting yeast cell growth *in vivo*. J. Biol. Chem. *273*, 32254–32264.
17. Anandapadamanaban, M., Andresen, C., Helander, S., Ohyama, Y., Siponen, M.I., Lundström, P., Kokubo, T., Ikura, M., Moche, M., and Sunnerhagen, M. (2013). High-resolution structure of TBP with TAF1 reveals anchoring patterns in transcriptional regulation. Nat. Struct. Mol. Biol. *20*, 1008–1014. https://doi.org/10.1038/nsmb.2611.
18. Miyasaka, S., Kitada, R., and Kokubo, T. (2023). Taf1 N-terminal domain 2 (TAND2) of TFIID promotes formation of stable and mobile unstable TBP-TATA complexes. Gene *889*, 147800. https://doi.org/10.1016/j.gene.2023.147800.
19. Gupta, K., Watson, A.A., Baptista, T., Scheer, E., Chambers, A.L., Koehler, C., Zou, J., Obong-Ebong, I., Kandiah, E., Temblador, A., et al. (2017). Architecture of TAF11/TAF13/TBP complex suggests novel regulation properties of general transcription factor TFIID. Elife *6*, e30395. https://doi.org/10.7554/eLife.30395.
20. Papai, G., Frechard, A., Kolesnikova, O., Crucifix, C., Schultz, P., and Ben-Shem, A. (2020). Structure of SAGA and mechanism of TBP deposition on gene promoters. Nature *577*, 711–716. https://doi.org/10.1038/s41586-020-1944-2.
21. Wang, H., Dienemann, C., Stützer, A., Urlaub, H., Cheung, A.C.M., and Cramer, P. (2020). Structure of the transcription coactivator SAGA. Nature *577*, 717–720. https://doi.org/10.1038/s41586-020-1933-5.
22. Birck, C., Poch, O., Romier, C., Ruff, M., Mengus, G., Lavigne, A.C., Davidson, I., and Moras, D. (1998). Human TAF(II)28 and TAF(II)18 interact

through a histone fold encoded by atypical evolutionary conserved motifs also found in the SPT3 family. [In Process Citation]. Cell *94*, 239–249.

23. Ben-Shem, A., Papai, G., and Schultz, P. (2021). Architecture of the multifunctional SAGA complex and the molecular mechanism of holding TBP. FEBS J. *288*, 3135–3147. https://doi.org/10.1111/febs.15563.
24. Lawson, K.A., Dunn, N.R., Roelen, B.A., Zeinstra, L.M., Davis, A.M., Wright, C.V., Korving, J.P., and Hogan, B.L. (1999). Bmp4 is required for the generation of primordial germ cells in the mouse embryo. Genes Dev. *13*, 424–436. https://doi.org/10.1101/gad.13.4.424.
25. Rivera-Pérez, J.A., and Magnuson, T. (2005). Primitive streak formation in mice is preceded by localized activation of Brachyury and Wnt3. Dev. Biol. *288*, 363–371. https://doi.org/10.1016/j.ydbio.2005.09.012.
26. Torres-Padilla, M.-E., Richardson, L., Kolasinska, P., Meilhac, S.M., Luetke-Eversloh, M.V., and Zernicka-Goetz, M. (2007). The anterior visceral endoderm of the mouse embryo is established from both preimplantation precursor cells and by *de novo* gene expression after implantation. Dev. Biol. *309*, 97–112. https://doi.org/10.1016/j.ydbio.2007.06.020.
27. Belo, J.A., Bouwmeester, T., Leyns, L., Kertesz, N., Gallo, M., Follettie, M., and De Robertis, E.M. (1997). Cerberus-like is a secreted factor with neutralizing activity expressed in the anterior primitive endoderm of the mouse gastrula. Mech. Dev. *68*, 45–57. https://doi.org/10.1016/s0925-4773(97)00125-1.
28. Niwa, H. (2007). How is pluripotency determined and maintained? Development *134*, 635–646. https://doi.org/10.1242/dev.02787.
29. Samanta, M., and Kalantry, S. (2020). Generating primed pluripotent epiblast stem cells: A methodology chapter. In Current Topics in Developmental Biology (Elsevier), pp. 139–174. https://doi.org/10.1016/bs.ctdb.2020.01.005.
30. Hayashi, K., Ohta, H., Kurimoto, K., Aramaki, S., and Saitou, M. (2011). Reconstitution of the Mouse Germ Cell Specification Pathway in Culture by Pluripotent Stem Cells. Cell *146*, 519–532. https://doi.org/10.1016/j.cell.2011.06.052.
31. Langer, D., Martianov, I., Alpern, D., Rhinn, M., Keime, C., Dollé, P., Mengus, G., and Davidson, I. (2016). Essential role of the TFIID subunit TAF4 in murine embryogenesis and embryonic stem cell differentiation. Nat. Commun. *7*, 11063. https://doi.org/10.1038/ncomms11063.
32. Kwan, J.Z.J., Nguyen, T.F., Uzozie, A.C., Budzynski, M.A., Cui, J., Lee, J.M.C., Van Petegem, F., Lange, P.F., and Teves, S.S. (2023). RNA Polymerase II transcription independent of TBP in murine embryonic stem cells. Elife *12*, e83810. https://doi.org/10.7554/eLife.83810.
33. Hnisz, D., Abraham, B.J., Lee, T.I., Lau, A., Saint-André, V., Sigova, A.A., Hoke, H.A., and Young, R.A. (2013). Super-enhancers in the control of cell identity and disease. Cell *155*, 934–947. https://doi.org/10.1016/j.cell.2013.09.053.
34. He, X.D., Phillips, S., Hioki, K., Majhi, P.D., Babbitt, C., Tremblay, K.D., Pobezinsky, L.A., and Mager, J. (2024). TATA-binding associated factors have distinct roles during early mammalian development. Dev. Biol. *511*, 53–62. https://doi.org/10.1016/j.ydbio.2024.04.002.
35. Martianov, I., Viville, S., and Davidson, I. (2002). RNA polymerase II transcription in murine cells lacking the TATA binding protein. Science *298*, 1036–1039.
36. Voss, A.K., Thomas, T., Petrou, P., Anastassiadis, K., Schöler, H., and Gruss, P. (2000). Taube nuss is a novel gene essential for the survival of pluripotent cells of early mouse embryos. Development *127*, 5449–5461.
37. Mohan, W.S., Jr., Scheer, E., Wendling, O., Metzger, D., and Tora, L. (2003). TAF10 (TAF(II)30) Is Necessary for TFIID Stability and Early Embryogenesis in Mice. Mol. Cell Biol. *23*, 4307–4318.
38. Tawamie, H., Martianov, I., Wohlfahrt, N., Buchert, R., Mengus, G., Uebe, S., Janiri, L., Hirsch, F.W., Schumacher, J., Ferrazzi, F., et al. (2017). Hypomorphic Pathogenic Variants in TAF13 Are Associated with Autosomal-Recessive Intellectual Disability and Microcephaly. Am. J. Hum. Genet. *100*, 555–561. https://doi.org/10.1016/j.ajhg.2017.01.032.
39. Santana, J.F., Collins, G.S., Parida, M., Luse, D.S., and Price, D.H. (2022). Differential dependencies of human RNA polymerase II promoters on TBP, TAF1, TFIIB and XPB. Nucleic Acids Res. *50*, 9127–9148. https://doi.org/10.1093/nar/gkac678.
40. Hisler, V., Bardot, P., Detilleux, D., Bernardini, A., Stierle, M., Sanchez, E.G., Richard, C., Arab, L.H., Ehrhard, C., Morlet, B., et al. (2024). RNA polymerase II transcription initiation in holo-TFIID-depleted mouse embryonic stem cells. Cell Rep. *43*, 114791. https://doi.org/10.1016/j.celrep.2024.114791.
41. Heinz, S., Benner, C., Spann, N., Bertolino, E., Lin, Y.C., Laslo, P., Cheng, J.X., Murre, C., Singh, H., and Glass, C.K. (2010). Simple combinations of lineage-determining transcription factors prime cis-regulatory elements required for macrophage and B cell identities. Mol Cell. *38*, 576–589. https://doi.org/10.1016/j.molcel.2010.05.004.
42. Zhang, Y., Liu, T., Meyer, C.A., Eeckhoute, J., Johnson, D.S., Bernstein, B.E., Nusbaum, C., Myers, R.M., Brown, M., Li, W., and Liu, X.S. (2008). Model-based analysis of ChIP-Seq (MACS). Genome Biol. *9*, R137. https://doi.org/10.1186/gb-2008-9-9-r137.
43. Martin, M. (2011). Cutadapt removes adapter sequences from high-throughput sequencing reads. EMBnet. j. *17*, 10. https://doi.org/10.14806/ej.17.1.200.
44. Dobin, A., Davis, C.A., Schlesinger, F., Drenkow, J., Zaleski, C., Jha, S., Batut, P., Chaisson, M., and Gingeras, T.R. (2013). STAR: ultrafast universal RNA-seq aligner. Bioinformatics *29*, 15–21. https://doi.org/10.1093/bioinformatics/bts635.
45. Langmead, B., and Salzberg, S.L. (2012). Fast gapped-read alignment with Bowtie 2. Nat. Methods *9*, 357–359. https://doi.org/10.1038/nmeth.1923.
46. Ramírez, F., Ryan, D.P., Grüning, B., Bhardwaj, V., Kilpert, F., Richter, A.S., Heyne, S., Dündar, F., and Manke, T. (2016). deepTools2: a next generation web server for deep-sequencing data analysis. Nucleic Acids Res. *44*, W160–W165. https://doi.org/10.1093/nar/gkw257.
47. Ye, T., Krebs, A.R., Choukrallah, M.A., Keime, C., Plewniak, F., Davidson, I., and Tora, L. (2010). seqMINER: an integrated ChIP-seq data interpretation platform. Nucleic Acids Res. *39*, e35.
48. Koressaar, T., and Remm, M. (2007). Enhancements and modifications of primer design program Primer3. Bioinformatics *23*, 1289–1291. https://doi.org/10.1093/bioinformatics/btm091.
49. Li, H., Handsaker, B., Wysoker, A., Fennell, T., Ruan, J., Homer, N., Marth, G.,Abecasis, G., Durbin, R., and 1000 Genome Project Data Processing Subgroup (2009). The Sequence Alignment/Map format and SAMtools. Bioinformatics 25, 2078–2079. https://doi.org/10.1093/bioinformatics/btp352.
50. Quinlan, A.R., and Hall, I.M. (2010). BEDTools: a flexible suite of utilities for comparing genomic features. Bioinformatics *26*, 841–842. https://doi.org/10.1093/bioinformatics/btq033.
51. Anders, S., Pyl, P.T., and Huber, W. (2015). HTSeq–a Python framework to work with high-throughput sequencing data. Bioinformatics *31*, 166–169. https://doi.org/10.1093/bioinformatics/btu638.
52. Hayashi, K., Ohta, H., Kurimoto, K., Aramaki, S., and Saitou, M. (2011). Reconstitution of the mouse germ cell specification pathway in culture by pluripotent stem cells. Cell *146*, 519–532. https://doi.org/10.1016/j.cell.2011.06.052.
53. Yamakawa, T., and Itakura, K. (2019). Chromatin Immunoprecipitation Assay Using Micrococcal Nucleases in Mammalian Cells. JoVE J. *59375*. https://doi.org/10.3791/59375-v.
54. Durinck, S., Moreau, Y., Kasprzyk, A., Davis, S., De Moor, B., Brazma, A., and Huber, W. (2005). BioMart and Bioconductor: a powerful link between biological databases and microarray data analysis. Bioinformatics *21*, 3439–3440. https://doi.org/10.1093/bioinformatics/bti525.

STAR★METHODS

KEY RESOURCES TABLE

REAGENT or RESOURCE	SOURCE	IDENTIFIER
Antibodies		
Mouse monoclonal anti-Oct3/4, IF	Santa Cruz	Cat# sc-5279; RRID: AB_628051
Mouse monoclonal anti-Dab2, IF	BD Biosciences	Cat# 610464
Mouse monoclonal anti-Cdx2, IF	Biogenex	Cat# AM392-5M; RRID: AB_2650531
Rabbit monoclonal anti-Cdx2, IF	Abcam	Cat# ab76541; RRID: AB_1523334
Rabbit polyclonal anti-Sox17, IF	Abcam	Cat# ab224637; RRID: AB_2801385
Rabbit polyclonal anti-Nanog, IF	Reprocell	Cat# RCAB002P-F
Mouse monoclonal anti-Taf13, WB	Santa Cruz	Cat# sc-393319
Rabbit polyclonal anti-Taf1, WB	Millipore	Cat# ABE42; RRID: AB_10863146
Goat polyclonal anti-Taf1, ChIP	Santa Cruz	Cat# sc-17134X; RRID: AB_2201077
Mouse monoclonal anti-Taf4, WB	In house	32TA-2B9, Langer et al.[31]
Mouse monoclonal anti-Taf4, Cut&Tag	Santa Cruz	Cat# sc-136093; RRID: AB_2199056
Mouse monoclonal anti-Taf7, WB	In house	19TA-2C7, Langer et al.[31]
Rabbit polyclonal anti-Taf10, WB	Santa Cruz	Cat# sc-102125; RRID: AB_2303129
Mouse monoclonal anti-Taf12, WB	In house	22TA-2A1, Langer et al.[31]
Rabbit polyclonal anti-Pol II, ChIP	Santa Cruz	Cat# sc-9001X; RRID: AB_2268548
Mouse monoclonal anti-Tbp, WB, IP, ChIP, Cut&Tag	Abcam	Cat# ab51841; RRID: AB_945758
Rabbit monoclonal anti-Tbp, WB, IP	Abcam	Cat# ab220788; RRID: AB_2927785
Rabbit monoclonal anti-H3K4Me3, ChIP	Millipore	Cat# 04-745; RRID:AB_1163444
Rabbit polyclonal anti-Xpb, Cut&Tag	Novus biologicals	Cat# NB100-61060; RRID: AB_925377
Rabbit polyclonal anti-H3K27ac, ChIP	Active Motif	Cat# 39133; RRID: AB_2561016
Rabbit anti-HA, ChIP	Sigma-Aldrich	Cat# H6908; RRID: AB_260070
Mouse monoclonal anti-β actine, WB	In house	N/A
Goat anti-Rabbit IgG (H + L) Highly Cross-Adsorbed Secondary Antibody, Alexa Fluor™ 488, IF	ThermoFisher Scientific	Cat# A11034; RRID: AB_2576217
Cy™3 AffiniPure™ Goat Anti-Mouse IgG (H + L), IF	Jackson ImmunoResearch	Cat# 115-165-003; RRID: AB_2338680
Peroxidase AffiniPure™ F(ab')$_2$ Fragment Goat Anti-Mouse IgG, Fcγ fragment specific, WB	Jackson ImmunoResearch	Cat# 115-036-071; RRID: AB_2338524
Peroxidase AffiniPure™ Goat Anti-Rabbit IgG (H + L), WB	Jackson ImmunoResearch	Cat# 111-035-144; RRID: AB_2307391
Chemicals, peptides, and recombinant proteins		
TRI Reagent (Trizol)	Molecular Research Center Inc.	Cat# TR188
PD0325901	Axon Medchem	Cat# 1408
CHIR99021	Axon Medchem	Cat# 1386
Leukemia inhibitory factor (LIF)	In house	N/A
L-Glutamine	GIBCO	Cat# 25030
N2 supplement	Invitrogen	Cat# 17502048
B27 supplement	Invitrogen	Cat# 17504-044
β-Mercaptoethanol	Sigma	Cat# M7522
Paraformaldehyde 16%	Electron Microscopy Sciences	Cat# 15710
Doxycycline Hydrochloride	MP Biomedicals	Cat# 195044
NP-40 (IGEPAL CA-630)	Sigma-Aldrich	cat# I3021
Complete Protease Inhibitor Cocktail (cOmplete), EDTA free	Roche	Cat# 11873580001
Protein G Sepharose	GE healthcare	Cat# 17-0618-05
Activin A	R&D systems	Cat# 338-AC-010

(*Continued on next page*)

Continued

REAGENT or RESOURCE	SOURCE	IDENTIFIER
FGF2	R&D systems	Cat# 233-FB-025
Purified BSA	New England BioLabs	Cat# B9001S
RNasine	Promega	Cat# N2111
VECTASHIELD Mounting Media without DAPI	VectorLabs	Cat# H-1000
Random Hexamer Primer	ThermoScientific	Cat# SO142
Critical commercial assays		
EdU proliferation kit (iFluor 488)	Abcam	Ab219801
LightCycler 480 SYBR Green 2X PCR Master Mix I	Roche	Cat# 4887352001
SuperScript IV Reverse Transcriptase	Invitrogen	Cat# 18090050
CUT&Tag-IT™ Assay Kit	Active Motif	Cat# 53160 (anti-rabbit), Cat# 53165 (anti-mouse)
CUT&Tag-IT® Spike-In Control, Anti-Rabbit	Active Motif	Cat# 53168 (anti-rabbit), Cat# 53173 (anti-mouse)
Nextera™-Compatible Multiplex Primers	Active motif	Cat# 53155
Sureguide kit	Agilent Technologies	Cat# 5190-7716
Venor™ GeM Mycoplasma Detection Kit	Merck	Cat# MP0025
Deposited data		
ChIP seq data	This study	GEO: GSE254025
mRNA seq data	This study	GEO: GSE254025
Cut&Tag seq data	This study	GEO: GSE254025
Experimental models: Cell lines		
J1	ATCC	cat# SCRC-1010
CD1 wt feeder cells	In house	N/A
J1 Taf13$^{-/-/Tg3XHATaf13+}$	This study	N/A
J1 Taf13$^{+/+/Tg3XHATaf13+}$	This study	N/A
Experimental models: Organisms/strains		
Taf13$^{+/-}$ mice	This study	N/A
C57BL/6N mice	JANVIER LABS	N/A
CD-1 mice	Charles River	N/A
Oligonucleotides		
For gRNA sequences, see Table S3	This study	N/A
For RT qPCR primers, see Table S4	This study	N/A
For ChIP qPCR primers, see Table S5	This study	N/A
For genotyping primers, see Table S6	This study	N/A
Recombinant DNA		
pX330.puro	Sandra Martha Gomes Dias Lab	Addgene plasmid #110403
pCW-Cas9	Eric Lander Lab	Addgene plasmid #50661
pCDH-CMV-MCS-EF1α-Puro	System Biosciences	Cat # CD510B-1
pLenti-TetON-puro	This study	N/A
Software and algorithms		
Homer	Heinz et al.[41]	http://homer.ucsd.edu/homer/
MACS2	Zhang et al.[42]	https://pypi.org/project/MACS2/
Cutadapt	Martin et al.[43]	https://cutadapt.readthedocs.io/en/v1.10/
STAR	Dobin et al.[44]	https://github.com/alexdobin/STAR
Bowtie	Langmead et al.[45]	https://bowtie-bio.sourceforge.net/bowtie2/index.shtml
deepTools	Ramírez et al.[46]	https://github.com/deeptools/deepTools
Picard Tools	Broad Institute	https://broadinstitute.github.io/picard/

(*Continued on next page*)

Continued

REAGENT or RESOURCE	SOURCE	IDENTIFIER
R	R-project	https://CRAN.R-project.org/
Prism (version 10)	GraphPad	N/A
seqMINER	Ye et al.[47]	N/A
Primer3	Koressaar et al.[48]	https://primer3.ut.ee/
Samtools	Li et al.[49]	http://samtools.sourceforge.net/
BEDTools	Quinlan et al.[50]	https://github.com/arq5x/bedtools
htseq-count	Anders et al.[51]	https://htseq.readthedocs.io/en/master/
Other		
DMEM (4,5 g/L Glucose) w/ GLUTAMAX medium	Life technologies	Cat# 31966-047
EmbryoMax Advanced KSOM Embryo Medium	Merck	Cat# MR-101-D
DMEM/F12 medium	Gibco	Cat# 11330-032
Neurobasal media	Gibco	Cat# 21103-049
BM-Purple	Roche	Cat# 11442074001
Blocking reagent	Roche	cat #11096176001

EXPERIMENTAL MODEL AND STUDY PARTICIPANT DETAILS

Generation of Taf13 knock out mice

Animal care, use, and experimental procedures were conducted in accordance with recommendations of the European Community (86/609/EEC), European Union (2010/63/UE) and the French National Committee (87/848). Taf13 knock out mice were generated by PHENOMIN-ICS at the Mouse Clinic Institute, France (http://www.phenomin.fr) using CRISPR Cas 9 technology. Two 5' (gR80 = GCGUUUAAUCCUAGUUGGUA and gR59 = CAUUGGUCAGUCUCUGAGUC) and two 3' (gR70 = AAAGUGCUAGUGUUGU CUAA and gR61 = ACCAGGAACUUGCACAAAGC) guide RNAs, sgRNA numbers refer to the MIT specificity score (https://crispor.tefor.net/crispor.) were designed to delete exon 3 (ENSMUSE00001293652) of the gene coding for Taf13 and their efficiency validated *in vitro* using the Sureguide kit (Agilent Technologies 5190-7716). All 4 gRNA were injected into fertilized C57BL/6N oocytes together with RNA coding for WT Sp-Cas9. Injected eggs were re-implanted into CD1 pseudo-pregnant females. Three founder males were identified by PCR screening of born pups using the following primers: Fwd= AGCCTGGACCAAACCAGGTCC and Rv= CTCTGGCCTCTGAGAGAACCA to detected deletion of exon 3. Positive males were used to determine germ line transmission and then used to establish two Taf13 knock out mice lines designated lines 11 and 25.

Generation of mESC lines

Taf13 knock out ESCs were generated by deletion of exon 3 using CRISPR Cas 9 technology. Guide RNAs targeting the regions 5′ and 3′ of exon 3 (CTGGGCATGGTACTATT and AGTGCTAGTGTTGTCGAA) were cloned into modified pX330.puro (Addgene #110403) plasmid containing two U6 promoters to express gRNAs and Sp-Cas9 nuclease cDNA under control of the CMV promoter. J1 ESCs (ATCC, cat# SCRC-1010, male) were co transfected with Cas9 expressing plasmid and a pLenti-TetON-puro plasmid, designed by replacing Cas9 sequence in pCW-Cas9 (Addgene #50661) by multiple cloning sites NheI-BmtI-SalI-EcoRI-BamHI expressing 3XHA-tagged Taf13 under control of a tight Tet-responsive promoter and cultured in the presence of puromycin and doxycycline until puromycin resistant clones were isolated. 20 clones were picked and amplified to verify deletion of both alleles and ectopic expression of 3XHA-Taf13. Two positive clones were identified by PRC and the absence of Taf13 confirmed by loss of Taf13 protein on immunoblots with one clone chosen for further experiments.

Taf13 ChIP was performed in J1 ESCs stably expressing ectopic 3XHA-Taf13 under control of the CMV promoter. To establish this line, ESCs were transfected with a pCDH-CMV-MCS-EF1α-Puro plasmid (System Biosciences, #CD510B-1) expressing 3XHA-Taf13 and puromycin resistant clones were isolated and amplified. Expression of 3XHA tagged Taf13 was verified by western blot.

METHOD DETAILS

Cell culture, growth and differentiation

J1 ESCs were cultured on inactivated MEF feeders under standard conditions (DMEM 4.5 g/L glucose/Glutamic supplemented with 15% heat inactivated FCS, LIF, nonessential amino acids and β-mercaptoethanol). Cells were regularly tested using the Venor GeM Mycoplasma Detection Kit. Proliferation was measured using EdU proliferation kit (Abcam, ab219801 (iFluor 488). For spontaneous differentiation, ESCs were feeder depleted and allowed to form EBs in DMEM 4.5 g/L glucose/Glutamax supplemented with 10% heat inactivated FCS, nonessential amino acids and β-mercaptoethanol in non-adherent bacterial plates. EBs were cultured for a

total of 14 days with medium change every other day. Differentiation into EpiLC was performed as described.[29] Briefly, cells were cultured for 7 days in the absence or presence of doxycycline in a standard medium described above supplemented with 2i. After 7 days cells were feeder depleted and cultured in serum free N2B27 medium (DMEM/F12 (Gibco#11330-032): Neurobasal media (Gibco#21103-049) = 1:1, 2 mM L-Glutamine (GIBCO#25030), 0.1 mM β-Mercaptoethanol (Sigma#M7522), 1X N2 supplement (Invitrogen#17502048), 1X B27 supplement (Invitrogen#17504-044)) supplemented with 2i (1 μM PD0325901 (Axon Medchem, #1408) and 3 μM CHIR 99021, (Axon Medchem, #1386)) and LIF (2X) for another 6 days in the absence or presence of doxycycline. Cells were trypsinised and seeded into plates in the same medium where 2i and LIF were replaced by Activin A (R&D systems, 338-AC-010) and FGF2 (R&D systems, 233-FB-025). Cells were cultured for 3 days in the absence or presence of doxycycline.

Blastocyst isolation and culture

Taf13 heterozygous mice were crossed and E3.5 blastocysts were flushed out the uterus in a standard ESC culture medium (see above) and cultured in EmbryoMax Advanced KSOM Embryo Medium (Merck, MR-101-D) for 24 h prior to immunostaining.

Histology and whole mount *in situ* hybridization

Deciduae were fixed in Bouin's fluid for 14h before being dehydrated and embedded in paraffin. The embedded decidua were cut in 5μm sections and stained with hematoxylin and eosin. Mouse embryos were dissected in ice-cold PBS and fixed O/N in 4%PFA/PBS. After several washes in PBS-0.1% Tween-20 (PBT) to eliminate traces of formaldehyde, embryos were bleached for 1h in 3% H2O2/PBT and washed 3 × 5 min in PBT before being digested with Proteinase K (10ug/ml) for 30 s. Digestion was stopped by 5 min incubation in 2 mg/ml glycine/PBT. Embryos were washed again 3 × 5 min in PBT before post-fixing for 20 min in 0.2% glutaraldehyde/4% PFA/PBS. After further washes they were incubated in prewarmed hybridization buffer (50% formamide, 5X SSC, 1% SDS, 100 μg/mL tRNA, 50 μg/mL heparine in water) and prehybridized for 2h at 65°C. The buffer was then replaced with fresh prewarmed hybridization buffer containing the digoxigenin labeled RNA probes and incubated O/N at 65C. The next day, embryos were washed twice in the hybridization buffer at 65°C before treating them with RNaseA to reduce background. The embryos were then blocked for 2h in 2% blocking reagent (Roche, cat #11096176001)/TBS- 0.1% Tween-20 (TBST) and incubated O/N in the same solution containing 1:2500 anti-digoxigenin antibody (Roche). The next day the embryos were washed in TBST, before washing them in NTMT buffer (100 mM NaCl, 100 mM Tris–HCl (pH 9.5), 50 mM MgCl2, and 0.1 % Tween 20 in water) (2 × 10 min) and developing the signal with BM Purple (Roche).

Immunostaining

Embryo deciduae were fixed overnight in 4% paraformaldehyde, washed with PBS, dehydrated, paraffin embedded, and sectioned at 5 μm. Prior to staining, sections were deparaffinized and boiled for 3 min in 10 mM of sodium citrate buffer for antigen retrieval. Sections then were permeabilized with 2 × 10 min 0.1% Triton in PBS, blocked for 30 min in 5% Normal Goat Serum (NGS) in PBS, and incubated overnight in 5% NGS with primary antibodies. Sections were washed 2 × 10 min 0.1% Triton in PBS, and incubated with secondary antibodies. Sections were washed 2 × 10 min 0.1% Triton in PBS, 1 × 5 min in PBS and incubated with DAPI (1 μg/mL) for 10 min, washed 3 × 5 min in PBS and mounted with Vectashild. For immunostaining, blastocysts were fixed in 4% paraformaldehyde for 15 min, washed briefly in PBS, permeabilized with 2 × 10 min 0.1% Triton in PBS, blocked for 30 min in 10% NGS and incubated with primary antibody overnight. Blastocysts were washed 2 × 10 min 0.1% Triton in PBS and incubated with secondary antibody for 1 h at room temperature. Washed again 2 × 10 min 0.1% Triton in PBS, 1 × 5 min in PBS and incubated with DAPI (1 μg/mL) for 10 min, washed 3 × 5 min in PBS. Embryos were placed individually into PBS drops under mineral oil in 6 cm petri dishes and images were acquired on an inverted Leica DMI8 confocal microscope. Primary antibodies: mouse anti-Oct4 (Santa Cruz, sc-5279), mouse anti-DAB2 (BD Biosciences, 610464), rabbit anti-CDX2 (Abcam ab 76541), mouse anti-CDX2 (Biogenex, AM392-5M), rabbit anti-SOX17 (Abcam, ab224637), rabbit anti-Nanog (Reprocell, RCAB002P-F). Secondary antibodies: goat Anti-Mouse IgG (H + L) Cy™3 (Jackson ImmunoResearch, 115-165-003), Goat anti-Rabbit IgG (H + L) Alexa Fluor™ 488 (ThermoFisher Scientific, A11034).

Genotyping of blastocysts and later stage embryos

Blastocysts at E3.5 or E4.5 were digested for 12 hs at 55°C in 10 μL TPB buffer containing proteinase K (0.2 mg/mL) (10X TPB buffer: 100 μM KCl, 200 μM Tris pH 8,8, 100 μM (NH4)2SO4, 20 μM MgSO4, 1% Triton X-100). Proteinase K was heat inactivated at 95°C for 5 min and the totality of the sample used directly for 40 cycles of PCR using Fwd and Rv primers. E6.5 - E8.5 embryos were digested in 20 μL TPB buffer with proteinase K as described above. 2 μL of digestion were used for 30 cycles of PCR.

Preparation of ESC nuclear extracts, immunoprecipitation, gel filtration and immunoblot

ESCs were resuspended in swelling buffer (25 mM Tris pH 7,9, 10 mM KCl, 1.5 mM MgCl2, 1 mM DTT), incubated for 10 min on ice, lysed using a dounce homogeniser and centrifuged. Pelleted nuclei were resuspended in extraction buffer (50mM Tris pH 7.5, 500 mM KCl, 0.5% NP-40 (IGEPAL CA-630) (Sigma-Aldrich, cat# I3021), 5% Glycerol and 1×Roche complete protease inhibitor) and proteins were extracted for 2h at 4°C with rotation. For immunoprecipitation, 200 μg nuclear extract were pre-cleared for 2 h with 50 μL of protein G sepharose beads, before addition of 3 μL of anti-TBP (Abcam, ab220788) antibody O/N at 4°C. The next day, bound complexes were recovered by incubating the extract with 20 μl protein G sepharose beads for 2 h at 4°C. Beads

containing bound proteins were washed 1 time with low salt buffer (100 mM KCl, 50 mM Tris pH8, 20% glycerol, 0.1% NP-40), 2 times with high salt buffer (500 mM KCl, 50 mM Tris pH8, 20% glycerol, 0.1% NP-40) and 1 time with low salt buffer before being boiled in SDS loading buffer for 5 min at 95°C. 500 ul of nuclear extracts prepared as described above containing 6 mg of protein were injected onto a equilibrated Superose 6 (10/300) column and run at 0.4 ml/min 500ul fractions were collected and analyzed by western blot. Proteins were analyzed by Western blot using the indicated antibodies: mouse anti-Taf13(Santa Cruz, sc-393319), rabbit anti Taf11 (Proteintech, 16114-1-AP), rabbit anti-HA (Sigma-Aldrich, H6908), rabbit anti-Taf1 (Millipore, #ABE42), rabbit anti-Taf10 (Santa Cruz, sc-102125). Antibodies against Taf4, Taf6, Taf7, and Taf12 are in house produced. Images were captured using an Amersham™ Imager 600.

RNA preparation, quantitative PCR and RNA-seq

Total RNA isolation was performed using Tri Reagent (Molecular Research Center, TR118) according to manufecturer's instruction. qRT-PCR was carried out with SYBR Green I (Roche) and SuperScript IV Reverse Transcriptase (Invitrogen) and monitored using a LightCycler 480 (Roche). Expression of Rplp0 gene was used to normalize the results. In a case of differentiation into EpiLC, expression of Oct4 was used as standard as Rplp0 was strongly down-regulated in cells cultured in serum free 2i medium whereas Oct4 expression was stable[52] Primer sequences for each cDNA were designed using Primer3 Software are shown in Table S2.

RNA-Seq libraries were generated from 800 ng of total RNA using TruSeq Stranded mRNA Library Prep Kit and IDT for Illumina - TruSeq RNA UD Indexes (96 Indexes, 96 Samples) (Illumina, San Diego, USA), according to manufacturer's instructions. Briefly, following purification with poly-T oligo attached magnetic beads, the mRNA was fragmented using divalent cations at 94°C for 2 min. The cleaved RNA fragments were copied into a first strand cDNA using reverse transcriptase and random primers. Strand specificity was achieved by replacing dTTP with dUTP during second strand cDNA synthesis using DNA Polymerase I and RNase H. Following addition of a single 'A' base and subsequent ligation of the adapter on double stranded cDNA fragments, the products were purified and amplified with PCR to create the cDNA library. Surplus PCR primers were further removed by purification using SPRI select beads (Beckman-Coulter, Villepinte, France) and the final cDNA libraries were checked for quality and quantified using capillary electrophoresis. After single strand sequencing on an Illumina HiSeq4000 sequencer, image analysis and base calling were performed using RTA version 2.7.7 and bcl2fastq version 2.20.0.422. Reads were preprocessed in order to remove adapter, polyA and low-quality sequences (Phred quality score below 20). After this preprocessing, reads shorter than 40 bases were discarded for further analysis. These preprocessing steps were performed using cutadapt version 1.10. Reads were mapped onto the mm10 assembly of Mus musculus genome using STAR version 2.5.3a. Gene expression quantification was performed from uniquely aligned reads using htseq-count version 0.6.1p1, with annotations from Ensembl version 102 and "union" mode.

Chromatin preparation, chromatin immunoprecipitation, sequencing and analysis

MNase-digested chromatin was prepared as described in.[53] Cells were fixed with 1% of PFA for 10 min directly in Petri dishes. Cross-linking was stopped with 125 mM glycine, cells were scrapped and centrifuged in a 50 mL tube at 9000g. MNase digestion was performed on a 100 μL cell pellet. Cells were permeabilised in 300 μL of MNase ChIP lysis buffer (1.512 g/L PIPES , 85 mM KCl, 0.5% NP-40 (IGEPAL CA-630, Sigma-Aldrich, cat# I3021) and 1X Complete Protease Inhibitor Cocktail (Roche, Cat# 11873580001)) for 10 min at 4°C. After centrifugation for 3 min at 9000 g, the pellet was resuspended in 300 μL cold MNase reaction buffer (50 mM Tris HCl pH8, 5 mM CaCl2, 0.1 ug BSA, 1 mM DTT. 3μL MNase (NEB, 2000 gelU/uL, cat #M0247S) were added to the suspension and incubated for 10 min at 37°C. To stop reaction 30 μL 0.5M EDTA was added and incubated on ice for 5 min. Cells were centrifuged and the pellet was resuspended in 300 μL ChIP dilution buffer (16.7 mM Tris HCl pH8, 0.01% SDS, 1.1% Triton X-100, 1.2 mM EDTA, 167 mM NaCl) and briefly sonicated (for 30 s) on E220 Focused-ultrasonicator (Covaris). Suspension was centrifuged for 10 min at 9000g. Supernatant is the MNase digested chromatin.

To prepare sonicated chromatin, cells were fixed in 0.4% PFA for 10 min and reaction was stopped by adding 125 mM glycine. 100 μL of cell pellet was lysed in 500 μL cell lysis buffer (1% SDS, 10 mM EDTA, 50 mM Tris pH8) and sonicated on E220 Focused-ultrasonicator (Covaris) for 10 min.

Size of sheared DNA was monitored on 1% agarose gel. ChIP experiments were performed on MNase-digested chromatin (for HA, TBP and Taf1) and sonicated chromatin (for Pol II, H3K4Me3 and H3K27ac). ChIP samples were purified using SPRIselect beads (Beckman-Coulter, Villepinte, France) and quantified using the Qubit 4 fluorimeter (Thermo Fischer Scientific, Illkirch, France). ChIP-seq libraries were prepared from 0.1 to 7 ng of double-stranded purified DNA using the MicroPlex Library Preparation kit v3 (C05010001, Diagenode, Seraing, Belgium), according to manufacturer's instructions. In the first step, the DNA was repaired and yielded molecules with blunt ends. In the next step, stem-loop adaptors with blocked 5 prime ends were ligated to the 5′ end of the genomic DNA, leaving a nick at the 3-prime end. The adaptors cannot ligate to each other and do not have single-strand tails, avoiding non-specific background. In the final step, the 3 prime ends of the genomic DNA were extended to complete library synthesis and Illumina compatible indexes were added through a PCR amplification (10 + 4 cycles). Amplified libraries were purified and size-selected using SPRIselect beads (Beckman Coulter) to remove unincorporated primers and other reagents. Image analysis and base calling were performed using RTA and bcl2fastq.

Sequence reads were mapped to reference genome mm10 using Bowtie 1.1.2 with the following parameters –no-unal -m 1 –seedlen 40 –best –strata –chunkmbs 1024 –sam –tryhard. Wig and BigWig files were generated using Homer[41] makeUCSCfile v4.11.0 with default parameters except for "-norm 2e7 -fragLength 200". Peak detection was performed using the MACS software v1.4.3 for

transcription factors and v2.1.1 in "broad" mode for chromatin marks.[42] Peaks were annotated with the 'annotatePeaks' command from HOMER v4.11 using the GTF annotation file from ENSEMBL v75. Motif search was performed with Homer findMotifsGenome tool at Galaxy France (https://usegalaxy.fr/). TATA motif search was performed with Homer scanMotifGenomeWide tool from the same source. Global clustering analyses with quantitative comparisons and representations of read density heatmaps were performed using seqMINER.[47] Visualization of ChIP-seq signal at specific gene loci of interest was achieved using the UCSC genome browser (https://genome.ucsc.edu/).

Cut & Tag

Cut and Tag experiments were carried out on 200 000 live cells using CUT&Tag-IT™ Assay Kit (Active motif, Catalog No. 53165 for TBP and Taf4, and No. 53160 for Xpb) according to the manufacturer's instructions. 10 000 Drosophila nuclei (5%) (Active motif, Catalog No. 53173 for TBP and Taf4 and No. 53168 for XPB) were added as spikes to each sample at the same time as Concanavalin A Beads. Libraries were prepared according to the Active motif CUT&Tag-IT™ Assay Kit manufacture's manual (Catalog No. 53165 and No. 53160) using Nextera™-Compatible Multiplex Primers (Active motif, Catalog No. 53155). After sequencing, reads were mapped onto the mm10 assembly of Mus musculus genome using bowtie2[45] version 2.2.6 (–phred33 –end-to-end –no-mixed –no-discordant -I 10 -X 700 –mm –very-sensitive). After alignment, reads were filtered using samtools view version 1.7 with the following parameters: -f 2 -F 1804 -q 10. Then duplicate reads were tagged using MarkDuplicates version 2.18.4 from Picard tool suite (B. Institute, \Picard tools. http://broadinstitute.github.io/picard/, 2018). BigWig files were generated using makeUCSCfile v4.11.0 with the following parameters -norm 3963942.

For normalization, spike in reads were mapped to Drosophila genome (BDGP6) using Bowtie2 v2.5.0 with default parameters except for "-X 2000". BigWig files were generated using Deeptools bamCoverage[46] v3.5.4 with the following parameters "-bs 10 -p 10 –skipNonCoveredRegions –extendReads –ignoreDuplicates —scaleFactor N where scale factors values are determined based on drosophila mapped reads.

Pausing index

Pausing index was defined as 5′ read density/gene body density. Gene positions were extracted from Ensembl v102 using R scripts and the R/Bioconductor package biomaRt v2.50.0. The number of reads per gene body and 5′ region was counted using BEDtools intersect v2.30.0. The 5′ region of genes was defined between TSS-30nt and TSS +300nt. Gene body region was defined as the region comprised between TSS +301nt and TTS-300nt. Gene Bodies were all normalized to be 1000nt long. Moreover, 1 was added to the gene body and 5′ read counts so that illegal division could not occur.[50,54] *p*-values were calculated by Wilcoxon signed-rank test.

QUANTIFICATION AND STATISTICAL ANALYSIS

Details for individual experiments including number of biological, technical replicates and statistical tests performed can be found in the figure legends. Comparisons were considered statistically significant with a p.value < 0.05: $*p < 0.05$, $**p < 0.01$, $***p < 0.001$, $****p < 0.0001$. Western blots were quantified using an Amersham Imager 600. Statistical analyses of data presented in Figures 1, 2, and 4 were performed using Graphpad Prism 10.